Article

Developmental Cell

Maturation and Clearance of Autophagosomes in Neurons Depends on a Specific Cysteine Protease Isoform, ATG-4.2

Highlights

- Retrograde transport of autophagic vacuoles requires the motor adaptor UNC-16/JIP3
- Protease ATG-4.2, but not related ATG-4.1, is required for autophagosome maturation
- ATG-4.2 cleaves LGG-1/Atg8 to remove it from membranes and enable lysosomal fusion
- Transport and maturation mechanisms interact to clear autophagosomes from synapses

Authors

Sarah E. Hill, Karlina J. Kauffman, Mia Krout, Janet E. Richmond, Thomas J. Melia, Daniel A. Colón-Ramos

Correspondence

daniel.colon-ramos@yale.edu

In Brief

Hill et al. use genetic screening and live imaging of autophagosomes in *C. elegans* to observe activity-dependent synaptic autophagy and discover that autophagosome trafficking and clearance are coordinated in neurons. They discover a unique role for protease isoform ATG-4.2 in cleaving LGG-1/Atg8/GABARAP from autophagosomes to promote their maturation and clearance.

Hill et al., 2019, Developmental Cell *49*, 1–16
April 22, 2019
https://doi.org/10.1016/j.devcel.2019.02.013

CellPress

Please cite this article in press as: Hill et al., Maturation and Clearance of Autophagosomes in Neurons Depends on a Specific Cysteine Protease Isoform, ATG-4.2, Developmental Cell (2019), https://doi.org/10.1016/j.devcel.2019.02.013

Developmental Cell
Article

Maturation and Clearance of Autophagosomes in Neurons Depends on a Specific Cysteine Protease Isoform, ATG-4.2

Sarah E. Hill,[1,2] Karlina J. Kauffman,[2] Mia Krout,[3] Janet E. Richmond,[3] Thomas J. Melia,[2] and Daniel A. Colón-Ramos[1,2,4,5,*]

[1]Department of Neuroscience, Program in Cellular Neuroscience, Neurodegeneration and Repair, Yale University School of Medicine, New Haven, CT 06510, USA
[2]Department of Cell Biology, Yale University School of Medicine, New Haven, CT 06510, USA
[3]Department of Biological Sciences, University of Illinois at Chicago, Chicago, IL 60607, USA
[4]Instituto de Neurobiología, Recinto de Ciencias Médicas, Universidad de Puerto Rico, 201 Blvd del Valle, San Juan 00901, Puerto Rico
[5]Lead Contact
*Correspondence: daniel.colon-ramos@yale.edu
https://doi.org/10.1016/j.devcel.2019.02.013

SUMMARY

In neurons, defects in autophagosome clearance have been associated with neurodegenerative disease. Yet, the mechanisms that coordinate trafficking and clearance of synaptic autophagosomes are poorly understood. Here, we use genetic screens and *in vivo* imaging in single neurons of *C. elegans* to identify mechanisms necessary for clearance of synaptic autophagosomes. We observed that autophagy at the synapse can be modulated *in vivo* by the state of neuronal activity, that autophagosomes undergo UNC-16/JIP3-mediated retrograde transport, and that autophagosomes containing synaptic material mature in the cell body. Through forward genetic screens, we then determined that autophagosome maturation in the cell body depends on the protease ATG-4.2, but not the related ATG-4.1, and that ATG-4.2 can cleave LGG-1/Atg8/GABARAP from membranes. Our studies revealed that ATG-4.2 is specifically necessary for the maturation and clearance of autophagosomes and that defects in transport and ATG-4.2-mediated maturation genetically interact to enhance abnormal accumulation of autophagosomes in neurons.

INTRODUCTION

Neurons are highly polarized cells in which autophagy is spatially compartmentalized. Local formation of autophagosomes is observed at the distal end of axons and at synapses (Maday and Holzbaur, 2014; Maday et al., 2012; Soukup et al., 2016; Stavoe et al., 2016). Synaptic autophagy can be enhanced under conditions of prolonged neuronal activity, suggesting a physiological link between neuronal activity and local autophagosome biogenesis (Shehata et al., 2012; Soukup et al., 2016; Wang et al., 2015). Autophagosomes are then transported toward the soma for lysosome fusion and degradation (Hollenbeck, 1993; Kaasinen et al., 2008).

Retrograde transport of autophagosomes is tightly controlled through both the recruitment and regulation of the dynein motor complex (Ikenaka et al., 2013; Katsumata et al., 2010; Maday et al., 2012; Neisch et al., 2017). Dynein is recruited to autophagosomes through fusion of autophagosomes with late endosomes (Cheng et al., 2015), and in vertebrate neurons, robust retrograde transport is facilitated by the motor scaffolding protein JIP1 (Fu et al., 2014). During transport, autophagic vacuoles (a general term encompassing autophagic structures of all maturity states [Klionsky et al., 2016]) begin progressive maturation (Maday et al., 2012; Neisch et al., 2017; Vanhauwaert et al., 2017), and once in the cell body, they are targeted for degradation and clearance through mechanisms that are not well understood. The importance of these regulated processes in neuronal autophagy is perhaps best exemplified by the consequences of their disruption, which include autophagosome accumulation at presynaptic terminals, Alzheimer's disease-like autophagic stress, and axonal pathology (Ikenaka et al., 2013; Lee et al., 2011; Nixon et al., 2005; Takáts et al., 2013; Tammineni et al., 2017).

In this study, we used forward and reverse genetics, combined with *in vivo* imaging, to identify mechanisms necessary for the clearance of synaptic autophagosomes. We visualized autophagosomes at single-neuron resolution by examining the localization of the autophagosome-associated protein LGG-1/Atg8/GABARAP (Manil-Segalen et al., 2014; Meléndez et al., 2003; Stavoe et al., 2016; Zhang et al., 2015). We found that, *in vivo*, we could predictably vary the number of synaptic autophagosomes by modulating the firing state of the neuron. We also detected synaptic proteins colocalized with autophagic vacuoles in the cell body, suggesting a link between autophagosome biogenesis at the synapse and autophagy-mediated degradation of synaptic proteins in the soma. We identified a role for the motor adaptor protein, UNC-16/JIP3, in facilitating robust retrograde transport of synaptic autophagic vacuoles to the cell body. To then uncover mechanisms that coordinate transport and elimination of autophagosomes from the neurite, we performed an enhancer screen in *unc-16/jip3*-mutant animals

and identified a dominant enhancer mutation in the poorly understood autophagy gene *atg-4.2*. Mutations in *atg-4.2; unc-16* double-mutant animals displayed dramatic accumulation of autophagosomes in the neurite, while *atg-4.2* single-mutant animals accumulated autophagosomes in the cell body, phenotypes not observed for the other *atg-4* gene in *C. elegans*, *atg-4.1*. We determined through biochemical assays that ATG-4.2 delipidates LGG-1 from membranes and observed that the accumulated autophagic vacuoles in *atg-4.2*-mutant animals failed to properly colocalize with lysosomal proteins, mature, and degrade. This resulted in a dramatic accumulation of abnormal multilamellar autophagosome-like vacuoles in the cell bodies of *atg-4.2*-mutant neurons. Our findings support a model in which the cysteine protease *atg-4.2* is specialized to remove LGG-1 and LGG-2 (hereafter LGG-1/LGG-2) from autophagosomes to enable autophagosome fusion with lysosomes and to promote degradation. Our studies uncover mechanisms that regulate transport and clearance of autophagosomes in neurites and provide a framework for understanding how disruption of trafficking and degradation genetically interact to result in abnormal accumulation of autophagosomes, as observed in neurodegenerative diseases.

RESULTS

Autophagosomes in *C. elegans* Neurons Contain Synaptic Proteins and Form Near Synapses in Response to Physiological Stimuli

To examine autophagy in neurons of living animals, we imaged LGG-1 and LGG-2 in the AIY interneurons of *C. elegans* at larval stage 4 (L4) (Figures 1A–1E and S1A–S1C, and as previously described in Stavoe et al. [2016]). LGG-1 and LGG-2 are *C. elegans* homologs of Atg8 (in yeast) and GABARAP and LC3 family proteins (in mammals) that associate with immature and mature autophagic structures and have been used as markers to track autophagosomes in living cells (Alberti et al., 2010; Manil-Segalen et al., 2014; Meléndez et al., 2003). For controls of these markers, please see Figures 1F, S1D–S1F, and STAR Methods).

Autophagosomes in AIY were present in the neurite (Figures 1B–1D) and in the cell body (Figure 1E). In the neurite, the majority of autophagosome biogenesis events occur near synaptic regions (Stavoe et al., 2016). To understand how activity of neurons relates to autophagosome biogenesis *in vivo*, we first examined autophagy in AIY neurons under varying physiological conditions. AIY is an interneuron that predictably changes its firing frequency based on inputs from sensory neurons (Laurent et al., 2015; Luo et al., 2014; Satoh et al., 2014). As part of its role in thermotaxis behavior, the frequency of calcium transients in AIY increases for animals raised at warmer temperatures (Clark et al., 2006; Hawk et al., 2018). We observed that animals raised at warmer temperatures, in which the neuronal activity state of AIY is increased, also had a higher percentage of animals with autophagosomes in AIY, and that this could be physiologically modulated by changing the cultivation temperature of the animals (Hawk et al., 2018; Figures 1G–1K). For example, in animals raised at 20°C, a condition known to lower AIY calcium activity (Hawk et al., 2018), the percentage of animals with one or more autophagosomes in either AIY neurite was 37% (n = 73 animals). When animals were cultivated at 25°C for 4 h, which is known to change their temperature preference through an increased calcium responsiveness of AIY, a concomitant increase in the percentage of animals with one or more autophagosomes in either AIY neurite was observed (81%) (n = 78 animals) (Figures 1G–1I). We do note that animals raised at warmer temperatures for prolonged periods of time, under conditions associated with noxious stimuli to the animal (and not known to be associated with thermotaxis behavior or increased activity states in AIY), also displayed an activity-independent increase in autophagosomes in the AIY neurite. Yet for the physiological conditions in which AIY is known to be active and required for thermotaxis behavior (exposure to higher temperatures for periods of less than 8 h), genetically inhibiting synaptic transmission suppressed the observed increase in synaptic autophagosomes (Figure 1J). Moreover, chemo-genetic silencing of AIY through the cell-specific expression of a histamine-activated chloride channel suppressed temperature-related increases in synaptic autophagosomes (Figure 1K). Previous findings using optogenetic approaches established a link between stimulation of the neuron and autophagosome biogenesis in the neurites (Shehata et al., 2012; Soukup et al., 2016; Wang et al., 2015). Our findings are consistent with and extend these studies, demonstrating that increases in autophagosomes near synapses can be induced by activity-dependent mechanisms associated with physiological responses of the neuron and activity-independent mechanisms associated with noxious stimuli to the system.

Does increased autophagy at active synapses act to recycle synaptic material? To address this, we examined if autophagic vacuoles in the cell body, where autophagosomes are transported for degradation, colocalized with synaptic proteins. Simultaneous visualization of active zone protein SYD-1 and autophagy-associated protein LGG-1 revealed partial colocalization in the neuronal cell body (Figures 1L–1N). Similar results were observed for active zone protein SYD-2/Liprin alpha and synaptic vesicle protein synaptobrevin (SNB-1) (Figures 1O–1Q and S1G–S1I). Our findings indicate that autophagic vacuoles in the cell body contain synaptic proteins and suggest that autophagy might degrade synaptic material such as active zone and synaptic vesicle proteins. Together, our findings are consistent with an association, *in vivo*, between the state of synaptic activity, the presence of autophagosomes at the synapse, and the degradation of synaptic material in the neuronal cell body.

Dynactin and JIP3/UNC-16 Promote Autophagosome Retrograde Transport

To then investigate how autophagosomes at the synapse are transported and degraded in the cell body, we recorded and tracked individual synaptic autophagosomes in wild-type and mutant animals. In *C. elegans* neurons, as in vertebrate neurons, retrograde transport of autophagosomes depends on the dynein complex (Cheng et al., 2015; Ikenaka et al., 2013; Katsumata et al., 2010; Maday et al., 2012) (Figures 2A–2C). We therefore examined known regulators of transport to investigate their specific requirement in autophagosome trafficking.

We observed that while available alleles for *jip-1/Mapk8Ip1-*, *unc-116/kinesin-1-,* and *unc-14/RUN*-mutant animals did not display defects in autophagosome accumulation at synapses (Figure 2G), loss of JIP3/UNC-16/Sunday Driver resulted in a

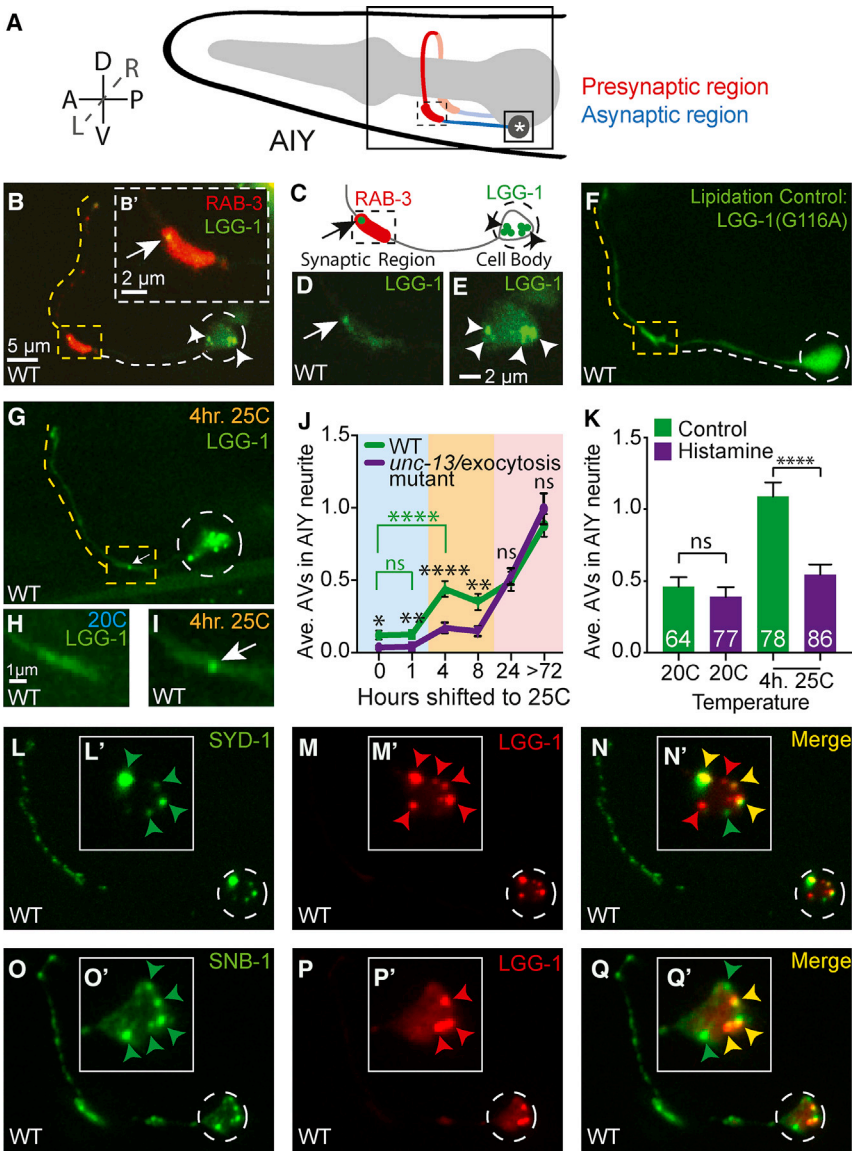

Figure 1. Synaptic Autophagosomes Occur in Response to Physiological Stimuli, and Cell Body Autophagosomes Contain Synaptic Material

(A) Schematic of the AIY interneuron pair located in the nerve ring within the head of the worm. Neurite (red and blue) and cell body (asterisk) are labeled. D, dorsal; V, ventral; A, anterior; P, posterior; L, left; R, right.

(B) Autophagosomes (visualized with GFP::LGG-1) in the synaptic regions (visualized with mCh::RAB-3) of a representative wild-type AIY interneuron. The dashed line traces the path of the AIY neurite (see schematic in 1A). The yellow dotted line highlights the synaptic regions of the neurite, and the white dashed line, the asynaptic region. The synapse-rich portion of the synaptic region (boxed) is enlarged in (B′).

(C) Schematic of AIY with the cell body and the proximal portion of the synaptic region as in (B).

(D) As in (B′) but GFP::LGG-1 only.

(E) Enlargement of the cell body in (B) and showing GFP::LGG-1 only. Note that we observe autophagic vacuoles in both the cell body and the synapse of neurons.

(F) LGG-1(G116A) fails to be lipidated and associated with autophagic vacuoles and does not form puncta at synapses or the cell body (Alberti et al., 2010; Manil-Segalen et al., 2014; Stavoe et al., 2016; see also Figure S1 for additional controls).

(G–I) Autophagosomes (visualized with GFP::LGG-1) in a representative wild-type AIY neuron held at 25°C for 4 h prior to imaging. In (H)–(I), the synaptic regions of wild-type AIY neurons are shown in animals held at 20°C (H) or held at 25°C (I) for 4 h prior to imaging. The AIY interneurons are primary interneurons in the thermotaxis circuit of *C. elegans*, and the activity state of AIY is known to increase when animals are held at 25°C for ~4 h (as compared to animals at 20°C) (Biron et al., 2006; Clark et al., 2006; Hawk et al., 2018). We therefore used the physiological stimuli of temperature in this intact circuit to increase the activity state of the AIY neurons and examine synaptic autophagy *in vivo* under these conditions. The synaptic-enriched region of (G) (dashed boxed) is enlarged in (I).

(J) Quantification of the average number of autophagosomes in the AIY neurite in wild-type (green line) and exocytosis/*unc-13(e450)*-mutant (purple line) animals. Animals were raised at 20°C and then held at 25°C for variable lengths of time as indicated. Note that after 4 h at 25°C, higher numbers of synaptic autophagosomes can be observed and that this increase is suppressed in exocytosis/*unc-13(e450)*-mutant animals (purple line). Our findings suggest that physiological increases in activity state of the neuron result in an increase in the number of synaptic autophagosomes. Our findings also demonstrate activity-independent increases in autophagosome number for animals raised at 25°C for 24 h or longer, likely due to temperature-dependent effects in the cell and consistent with the known detrimental effects of prolonged exposure of *C. elegans* to 25°C temperature conditions (Byerly et al., 1976; Hosono et al., 1982). For all genotypes and time points, the number of animals examined is $n \geq 45$. *$p < 0.05$, **$p < 0.01$, ****$p < 0.0001$, or "ns" not significant by Student's t test between wild-type and *unc-13*-mutant animals at each time point (black significance values) or between different wild-type time points (green significance values).

(K) Quantification of the average number of autophagosomes in the AIY neurite in animals expressing the heterologous *Drosophila* inhibitory chloride channel (HisCl) (Pokala et al., 2014) when exposed to the activating histamine (purple bars) or control (green bars). Error bars show standard error of the mean (SEM). ****$p < 0.0001$ by one-way ANOVA with Tukey's post hoc analysis between histamine and control conditions. The number of animals examined is shown on each bar.

(L–N) Representative confocal image of presynaptic active zone protein GFP::SYD-1 (L) colocalized with mCh::LGG-1 (M). Merged images shown in (N). Insets in (L′–N′) show the enlarged cell body with subcellular localization of these proteins.

(O–Q) As in (L)–(N), but imaging the subcellular localization of synaptic vesicle protein synaptobrevin (GFP::SNB-1) and mCh::LGG-1. Note how in both (L)–(N) and (O)–(Q), LGG-1 partially colocalizes in the cell body with synaptic proteins (also seen for active zone protein SYD-2 in Figures S1G–S1I).

Throughout the figures, images depict maximal projections of confocal z stacks, arrowheads refer to LGG-1 puncta in the cell body, arrows point to LGG-1 puncta in the synaptic regions, and dashed circles enclose cell bodies. Abbreviation: h, hours.

Scale bar(s) in (B) for (B), (F), (G), and (L)–(Q); in (B′) for (B′) and (D); in (E) for (E) and (L′)—(Q′); and in (H) for (H) and (I).

See also Figure S1.

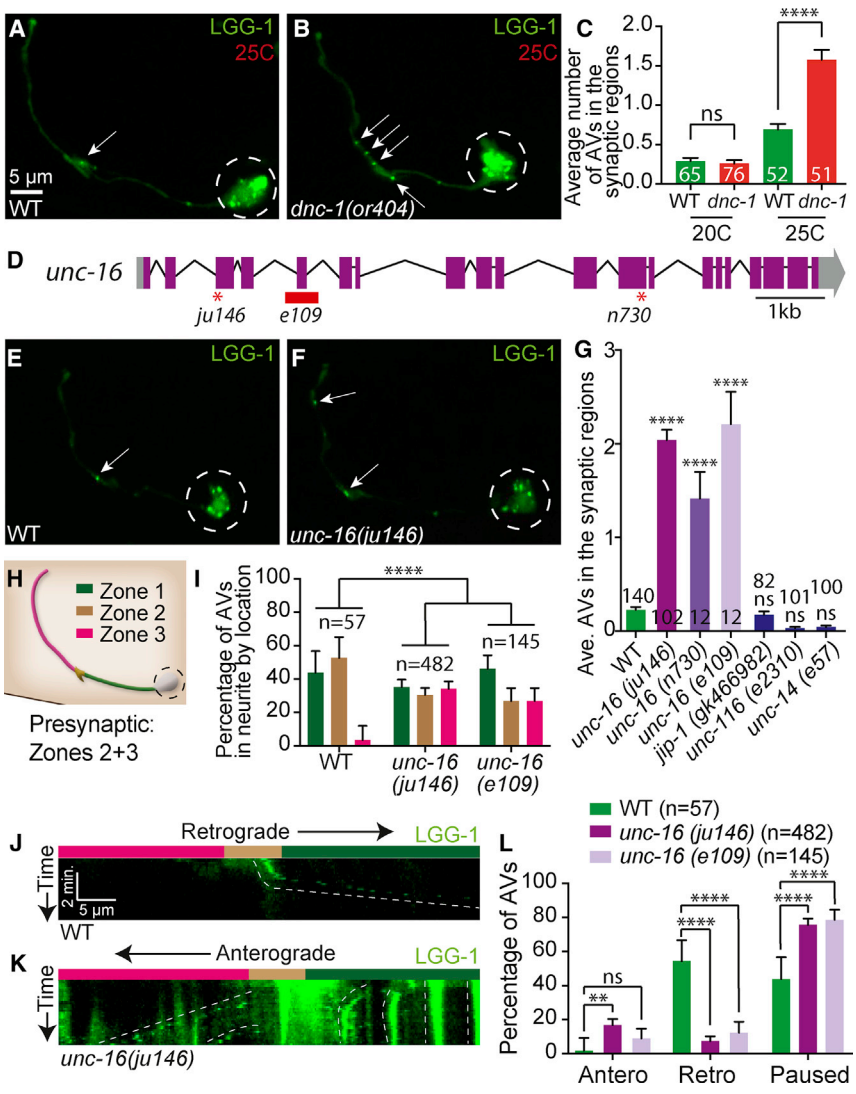

Figure 2. Dynactin and UNC-16/JIP3 Mediate Retrograde Transport of Autophagosomes from the Synaptic Regions

(A and B) Autophagosomes (visualized with GFP::LGG-1) in a wild-type AIY neuron (A) and in a temperature-sensitive dynactin, *dnc-1(or404)*-mutant animals (B) grown for 48 h at the restrictive temperature of 25°C.

(C) Quantification of the average number of autophagosomes in the synaptic regions in wild-type and *dnc-1(or404)*-mutant animals kept for 48 h at the permissive (20°C) or restrictive (25°C) temperature (note an increase in wild-type animals at 25°C, as in Figure 1J).

Error bars show standard error of the mean (SEM). ****p < 0.0001 by one-way ANOVA with Tukey's post hoc analysis between indicated groups. Numbers on bars represent number of animals examined.

(D) Schematic of the *unc-16*-genomic region with exons (purple boxes), untranslated regions (gray boxes), introns (black lines), and allelic lesions (early stop codons as red asterisks in *ju146* and *n730*; and deletion as red box in *e109*). Scale bar shows a 1-kilobase (kb) region.

(E and F) Autophagosomes (visualized with GFP::LGG-1) in a representative wild-type AIY neuron (E) and in an *unc-16(ju146)*-mutant neuron (F) grown at the standard 20°C.

(G) Quantification of the average number of autophagosomes in the synaptic regions in wild-type, three alleles of *unc-16*- (*ju146*, *n730*, and *e109*), *jip-1(gk466982)*-, *unc-116(e2310)*-, and *unc-14(e57)*-mutant animals. Error bars show standard error of the mean (SEM). ****p < 0.0001 by one-way ANOVA with Tukey's post hoc analysis. The number of animals examined is shown on each bar.

(H) Schematic of the AIY interneuron colored by region and similar to the schematic in Figure 1A. Zone 1, asynaptic, green; Zone 2, enriched-synaptic region, brown; Zone 3, punctate-synaptic region, pink; see Colon-Ramos et al., 2007. Modified and reprinted with permission from wormatlas.org.

(I) Quantification of the percentage of autophagosomes in the AIY neurite by location. Bars are colored as zones in (H). Zone-1-localized autophagosomes observed in wild-type animals many times represent synaptic autophagosomes in transit toward the cell soma. Error bars show a 95% confidence interval. ****p < 0.0001 by chi-square test between wild-type animals (n = 57 autophagosomes from 36 animals), *unc-16(ju146)*-mutant animals (n = 482 autophagosomes from 37 animals), and *unc-16(e109)*-mutant animals (n = 145 autophagosomes from 22 animals).

(J and K) Kymographs of autophagosome trafficking in AIY neurites in representative wild-type (J) and *unc-16(ju146)*-mutant (K) animals showing retrograde (right down diagonals), anterograde (left down diagonals), and paused events (vertical lines). Neurite zones are indicated by color above kymographs and as in (H).

(L) Quantification of autophagosome trafficking events in the AIY neurite, showing percentage of autophagosomes that undergo anterograde, retrograde, or paused events within the 5-min imaging window for wild-type and *unc-16*-mutant animals. ****p < 0.0001, **p < 0.01 by Fisher's exact test between wild-type and mutant animals. Error bars show a 95% confidence interval.

Arrows denote autophagosomes in the synaptic region. Dashed circles enclose the cell bodies. Abbreviations: ns, not significant; AV, autophagic vacuole. Scale bar(s) in (A) for (A), (B), (E), and (F); and in (J) for (J) and (K).

See also Figures S2 and S3.

significant accumulation of LGG-1/LGG-2 puncta in the neurite but not in the cell body (Figures 2E–2G and S2A–S2D). The *unc-16/jip3*- mutant phenotype was similar to the phenotype seen for *dnc-1/p150* dynactin-complex-subunit-mutant animals (which affect the dynein complex) (Ikenaka et al., 2013; Figures 2B and 2C). JIP3/UNC-16/Sunday Driver is a conserved adaptor protein that binds to kinesin and dynein (Arimoto et al., 2011; Cavalli et al., 2005) to regulate early endosome and lysosome transport (Brown et al., 2009; Byrd et al., 2001; Drerup and Nechiporuk, 2013; Edwards et al., 2013, 2015;; Gowrishankar et al., 2017). Mutant animals containing one of three independent alleles of *unc-16* (*ju146, e109*, or *n730*) (Figure 2D) displayed an increase in the percentage of animals with LGG-1 puncta in the neurites (from 34% in wild-type animals to 100% in all *unc-16*-allele-mutant animals examined). Moreover, while wild-type animals averaged less than one LGG-1 puncta per neurite, *unc-16*-mutant animals averaged ~2 LGG-1 puncta in the presynaptic regions (Figure 2G), indicating abnormal accumulation

of autophagosomes. Analyses of the subcellular localization of LGG-1-containing structures in *unc-16/jip3*-mutant animals also revealed a higher probability for autophagosomes to be present in the distal synaptic Zone-3 region (Figures 2H and 2I). The distal accumulation of autophagosomes observed for *unc-16*-mutant animals was not due to a rearrangement of microtubule polarity, as we observed that the microtubule plus-end-binding protein EBP-2/EB1 (Baas and Lin, 2011; Maniar et al., 2011) was similarly oriented (plus-end-out) in wild-type and *unc-16/jip3*-mutant animals (Figures S2E–S2G). Our findings indicate that *unc-16/jip3* is necessary to prevent the abnormal accumulation of autophagosomes in the neurite and are consistent with a requirement for *unc-16/jip3* in autophagosome retrograde transport.

Previous reports have implicated UNC-16/JIP3/Sunday Driver in the regulation of retrograde transport and retention of lysosomes, early endosomes, and Golgi in the cell body (Brown et al., 2009; Byrd et al., 2001; Edwards et al., 2013; Figure S3). The role of UNC-16/JIP3 in transport of autophagosomes has not been examined. To directly investigate if *unc-16/jip3* is required for retrograde transport of autophagosomes, we performed time-lapse imaging of individual LGG-1 puncta in wild-type neurons (n = 71) and for two independent alleles of *unc-16*-mutant neurons (*ju146*, n = 73; and *e109*, n = 43). We observed that compared to wild-type animals, *unc-16/jip3*-mutant animals displayed decreased retrograde transport of LGG-1 puncta in neurites and increased anterograde trafficking or paused LGG-1 puncta (defined as puncta that did not traffic within a 5-min observation window; Figures 2J–2L). In wild-type animals, LGG-1 puncta in the cell body were sometimes transported in an anterograde fashion into the neurite and returned to the cell body via retrograde transport within the 5-min examination window. In contrast, the percentage of puncta that returned was greatly reduced in *unc-16(ju146)*-mutant neurites (Figure S2H). Our findings are consistent with previous reports that demonstrate that another JIP family member (JIP1) is important for regulating autophagosome retrograde transport in cultured vertebrate neurons (Fu et al., 2014). We now extend those findings and demonstrate an important role for *unc-16/jip3* in regulating the retrograde trafficking of autophagosomes *in vivo*.

To understand how UNC-16-dependent retrograde transport contributes to the degradation of autophagic vacuoles, we then tested if defects in *unc-16*-mutant animals altered the total number of LGG-1 puncta in neurons. We observed that the total number of LGG-1 puncta in neurons of *unc-16/jip3*-mutant animals was higher than that seen for wild-type animals (average ± 95% confidence interval from 4.1 ± 0.6 in wild-type neurons (n = 65) to 8.2 ± 0.8 in *unc-16(ju146)*-mutant neurons (n = 64); significant by Student's t test $p < 0.0001$). Our findings indicate that the increased number of autophagic vacuoles observed in the neurites of *unc-16/jip3*-mutant animals did not result from a simple redistribution of a fixed number of autophagosomes. Instead, retrograde transport, promoted by *unc-16/jip3*, appears to be necessary for the effective degradation of autophagic vacuoles, and defects in transport in *unc-16/jip3*-mutant animals therefore result in an abnormal accumulation of autophagic vacuoles. Our findings underscore the importance of regulated trafficking in the degradation of synaptic autophagic vacuoles.

Mutant Allele *ola316* Enhances the Number of Autophagic Vacuoles in the Neurites of *unc-16/jip3*-Mutant Animals

Degradation of autophagosomes occurs upon fusion with lysosomes, an important and final step that is tightly regulated but poorly understood (Itakura et al., 2012; Nakamura and Yoshimori, 2017). To better understand the molecular machinery underlying coordinated trafficking and degradation of synaptic autophagic vacuoles, we performed a visual forward genetic screen in the *unc-16/jip3*-mutant background. We reasoned that molecules important for regulated lysosomal fusion and degradation would result in an enhanced accumulation of autophagosomes and screened for mutant animals with increased numbers of LGG-1 puncta in the AIY-synaptic regions. We uncovered a mutant allele, *ola316*, in which animals displayed a dramatic accumulation of LGG-1 puncta in the neurites. While *unc-16(ju146)*-mutant animals displayed an average of 2.6 LGG-1 puncta abnormally accumulated in the synaptic regions (n = 64 neurites), *ola316; unc-16(ju146)* double-mutant animals enhanced this phenotype and displayed an average of 9.4 LGG-1 puncta in the synaptic regions (n = 67 neurites) (Figures 3A–3D). We note that in these double-mutant animals with dramatic accumulation of autophagosomes, some LGG-1-positive structures were observed outside the AIY neurite (Figures S4A–S4C). It is possible that these LGG-1 structures might be expelled from the neurite in response to an overburdening of the endo-lysosomal system, a phenomenon known as "secretory autophagy" which has been observed in a number of contexts, including neurodegenerative diseases (Ponpuak et al., 2015; Borland and Vilhardt, 2017; Miranda et al., 2018; Ojha et al., 2017) (Video S1).

We then examined if animals containing the *ola316* allele displayed a phenotype independent of the *unc-16/jip3*-mutant lesion. To achieve this, we outcrossed the *ola316; unc-16(ju146)* animals to remove the *unc-16/jip3* lesion and examined LGG-1-containing structures in the *ola316* single-mutant animals. We observed that the *ola316* single-mutant animals did not display a significant accumulation of LGG-1 puncta in the synaptic regions when compared with *unc-16(ju146)*-mutant or *unc-16(ju146); ola316* double-mutant animals (Figure 3D). However, we did observe an increased number of LGG-1 puncta in the cell bodies of the *ola316* single-mutant animals (Figures 3E, 3H, and 3I; we observed similar results for LGG-2, Figures S4D, S4E, S4G, and S4H). We also observed an increase in the percentage of neurites with one or more LGG-1 puncta in the synaptic regions (Figure S4I). The gene affected in the *ola316* allele is important for most neurons in the nematode's nervous system, as abnormal pan-neuronal accumulation of LGG-1 puncta was observed for both the single-mutant animals and the *ola316; unc-16(ju146)* double-mutant animals (Figures S4J–S4Q). Together, our data indicate that the *ola316* allele affects a gene that is important for preventing the abnormal accumulation of autophagosomes both in the neuronal soma and, through cooperation with UNC-16/JIP3, in the neurites.

ola316 Is a Dominant Allele of the Autophagy Gene *atg-4.2*

Genetic characterization of animals containing the *ola316* allele revealed that the phenotype results from a single genetic dominant lesion (Figure 3E, green and red striped bar). To identify the

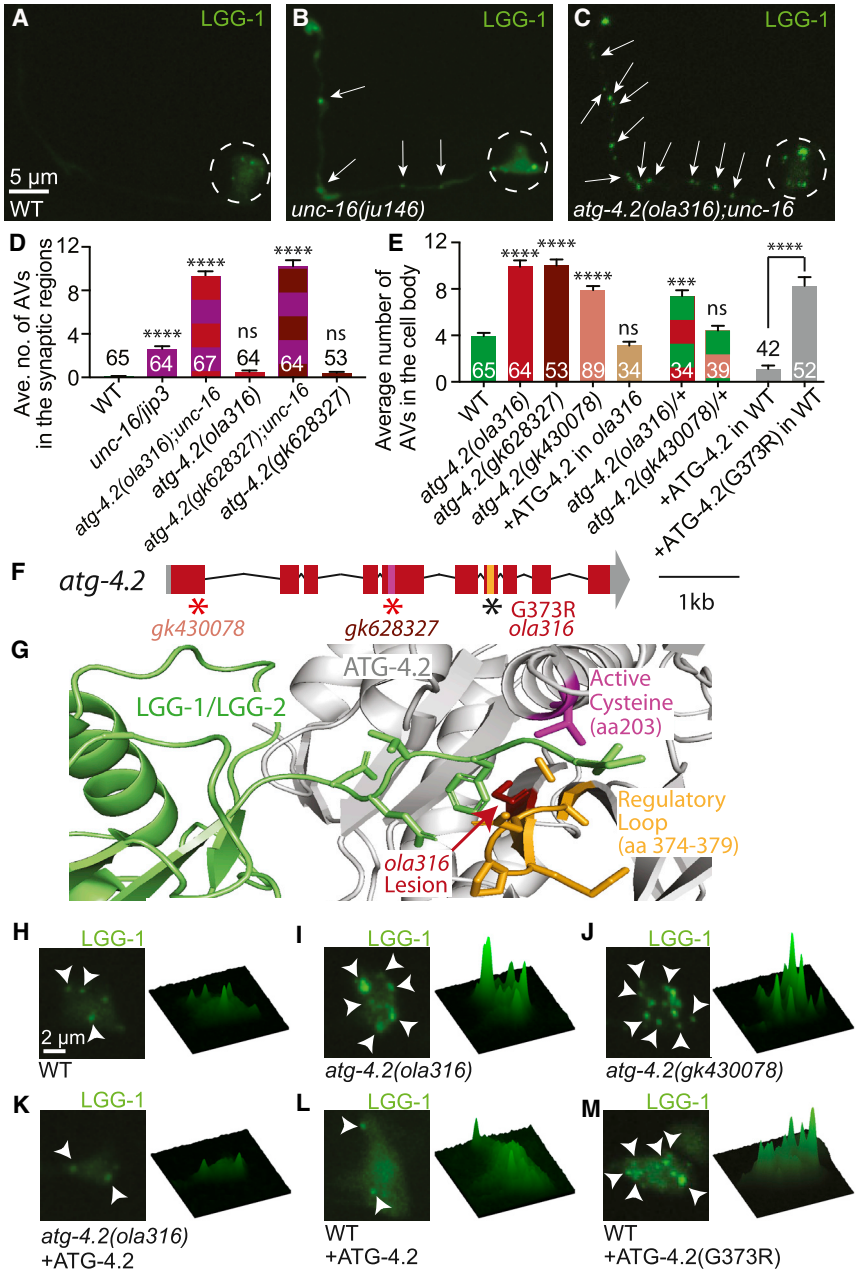

Figure 3. ATG-4.2 Enhances UNC-16/JIP3-Mediated Accumulation of Autophagosomes

(A–C) Autophagosomes (visualized with GFP::LGG-1) in representative wild-type (A), *unc-16(ju146)* mutant (B), and *atg-4.2(ola316); unc-16(ju146)* double-mutant (C) animals are shown.

(D and E) Quantification of the average number of LGG-1 puncta in the synaptic regions (Zones 2 + 3) of the AIY neurite (D) or in the cell body of AIY (E). Synaptic quantifications for wild-type, indicated mutant, and double animals are shown. Here *unc-16* refers to allele *ju146* (D). Cell body quantifications are shown for wild-type, indicated mutant animals, cell-specific expression of an ATG-4.2 rescuing array in *atg-4.2(ola316)*-mutant animals, heterozygous animals, and wild-type animals with AIY cell-specific expression of wild-type ATG-4.2 or mutant ATG-4.2 cDNA containing the lesion found in allele *atg-4.2(ola316)* (corresponding to [G373R]) (E). Error bars show standard error of the mean (SEM). ***$p < 0.001$; ****$p < 0.0001$ by one-way ANOVA with Tukey's post hoc analysis between wild-type and mutant animals. The numbers on the bars represent the number of neurons examined. See also Figure S1.

(F) Schematic of the *atg-4.2*-genomic region on chromosome IV with exons (red boxes), untranslated regions (gray boxes), and introns (black lines). Alleles affect indicated regions with early stop codons (red asterisks; *gk430078* and *gk628327*) or amino acid change (G373R for *ola316*). The conserved regulatory loop, important for substrate recognition (orange bar), and cysteine-active site (pink bar) are indicated. Scale bar shows a 1-kb region.

(G) Model of the crystal structure of the human ATG4B-LC3 complex (Kumanomidou et al., 2006) indicating the location of the G373R lesion from the *ola316* allele (red arrow), the conserved regulatory loop (orange) important for LC3 recognition (LGG-1/LGG-2, in green), and the cysteine- active site (pink, amino acid 203). Note that the G373R lesion in *atg-4.2(ola316)* neighbors the regulatory loop and is also sterically close to the active site in the three-dimensional predicted structure of the protein.

(H–M) Autophagic vacuoles in the AIY cell body imaged as maximal projection of confocal z stacks (left) and corresponding surface plots of the LGG-1 signal intensity (right) in wild-type animals (H), *atg-4.2(ola316)*-mutant animals (I), *atg-4.2(gk430078)*-mutant animals (J), *atg-4.2(ola316)*-mutant animals containing an ATG-4.2 rescue array (K), and wild-type animals cell-specifically overexpressing either ATG-4.2 (L) or ATG-4.2(G373R) (M).

Arrows denote autophagosomes in the neurite; arrowheads denote autophagic vacuoles in the cell body. Dashed circles enclose cell bodies. Abbreviations: ns, not significant; AV, autophagic vacuole. Scoring was done by blindly quantifying maximal projections of confocal z stacks.

Scale bar(s) in (A) for (A)–(C); in (H) for (H)–(M).

See also Figure S4.

causative lesion in animals containing *ola316*, we performed single-nucleotide polymorphism (SNP) mapping, whole-genome sequencing, independent allele analyses, and rescue experiments. We SNP-mapped *ola316* to a 2.2 megabase (Mb) region between 10.1 and 12.3 Mb on chromosome IV. We then performed whole-genome sequencing (Minevich et al., 2012; Sarin et al., 2008) and uncovered a missense lesion in the autophagy gene *atg-4.2*. Animals containing either of two independent alleles of *atg-4.2* (*gk430078* or *gk628327*), which result in early stop codons (Figure 3F), phenocopied the *ola316* single-mutant phenotype (Figure 3E (maroon and peach bars) and Figure 3J). Moreover, *unc-16(ju146); atg-4.2(gk628327)* double-mutant animals also phenocopied the *unc-16(ju146); ola316* double-mutant animals isolated from the genetic screen (Figure 3D). Consistent with *ola316* being an allele of *atg-4.2*, AIY-specific expression of the wild-type *atg-4.2* cDNA in *ola316*-mutant animals rescued the *ola316*-mutant phenotype (Figure 3E [brown bar], 3I and 3K). While this rescue experiment might suggest that the

dominant allele was acting through haploinsufficiency, we also observed that overexpression of mutant *atg-4.2(ola316)* cDNA in wild-type animals was sufficient to induce the phenotype (Figures 3E [gray bars], 3L and 3M), indicating that the *atg-4.2(ola316)* allele acts as a dosage-dependent dominant negative and that it is required cell autonomously in AIY. Our data indicate that *ola316* is an allele of the autophagy gene *atg-4.2* and that *atg-4.2* acts in neurons to regulate accumulation of autophagic structures.

Atg4s are a conserved family of cysteine proteases that bind to and cleave Atg8/GABARAP/LC3 /LGG-1/LGG-2 family proteins. Comparison with the human ATG4B-LC3 crystal structure (Kumanomidou et al., 2006) revealed that the *atg-4.2(ola316)* lesion identified in our screen neighbors a conserved regulatory loop important for LC3 (the vertebrate homolog of LGG-2) recognition by ATG4 (Wu et al., 2012) and is sterically close to the cysteine-active site (Figure 3G). Based on its position, and our *in vivo* genetic data, we hypothesize that the dominant lesion in the *atg-4.2(ola316)* allele might interfere with ATG-4.2 activity and its interaction with LGG-1/LGG-2.

Atg4s cleave Atg8/GABARAP/LC3/LGG-1/LGG-2 family proteins to achieve two functions: (1) prime LGG-1 (which contains a C-terminal tail) for conjugation onto the autophagosomal membrane, and (2) remove LGG-1 and LGG-2 from the autophagosomal membrane (Alberti et al., 2010; Kirisako et al., 2000; Maruyama and Noda, 2017). In yeast, one *ATG4* gene performs both the priming and delipidation events on Atg8/LGG-1/LGG-2 (Kirisako et al., 2000; Maruyama and Noda, 2017), while in higher metazoans, multiple genes encode distinct Atg4 cysteine proteases, some with unknown function, specificity, or redundancy (Kauffman et al., 2018; Li et al., 2011; Mariño et al., 2003; Wu et al., 2012; Zhang et al., 2016). Consistent with these, a previous study in *C. elegans* embryos determined that the two *C. elegans atg-4* genes (*atg-4.1* and *atg-4.2*) (Figure 4A) were largely redundant (Wu et al., 2012), with ATG-4.1 displaying enhanced proteolytic activity on a soluble pro-form of LGG-1/Atg8 as compared to ATG-4.2. The specific roles of ATG-4.2 in autophagy, if any, remain unknown.

ATG-4.2, but Not ATG-4.1, Is Required to Prevent Autophagosome Accumulation

The two *C. elegans* Atg4 homologs display 44% amino acid similarity, including conserved catalytic and regulatory sites (Wu et al., 2012). A previous study investigating the degradation of protein aggregates in embryos found that *atg-4.1* is more efficient at the first LGG-1 cleavage event (priming) and more important for the removal of protein aggregates than *atg-4.2* (Wu et al., 2012). To examine if *atg-4.1* also acts as *atg-4.2* to prevent autophagosomal accumulation in neurons, we examined animals containing a confirmed null allele of *atg-4.1*(bp501) (Wu et al., 2012) or containing the allele *atg-4.1*(gk127286) (early stop codon) (Figure 4A). Surprisingly, we did not detect LGG-1 or LGG-2 puncta accumulation in the *atg-4.1*-mutant animals (Figures 4C, 4E, S4F–S4H, and S4R).

We then examined autophagosomes in the neuronal cell bodies of these mutant animals by performing electron microscopy. Consistent with our GFP::LGG-1 and GFP::LGG-2 *in vivo* assays, we observed a dramatic accumulation of abnormal multilamellar autophagosome-like vacuoles in the neuronal somas of *atg-4.2(ola316)*-mutant animals (Figures 4F–4K and S5A–S5P). Our findings indicate that *atg-4.1* and *atg-4.2* have distinct functions *in vivo* that result in different phenotypes regarding the accumulation of autophagosomes in neurons. Importantly, our findings indicate that *atg-4.2* is specialized for the clearance of autophagic vacuoles.

While we observed distinct phenotypes for *atg-4.1* and *atg-4.2* in the accumulation of autophagic structures, we also note that both *atg-4.1* and *atg-4.2* single-mutant animals contained LGG-1/LGG-2 puncta in neurons (Figures 4C–4E and S4E–S4H). Comparisons with the corresponding lipidation controls (LGG-1(G116A); explanatory diagrams in Figure S1) suggest that nearly all of the observed LGG-1 puncta in *atg-4.1*- and *atg-4.2*-mutant animals were lipidated (Figures S5Q and S5T–S5V). These observations indicate that either protease is able to partially compensate for the absence of the other protease and perform the first priming cleavage necessary to conjugate LGG-1 onto the nascent autophagosome. They also localized similarly throughout the neuronal cytoplasm, consistent with the ability to act either in the synaptic region or the cell body (Figures S6A and S6B). Also consistent with these two proteases performing partially redundant roles, we have previously shown that in AIY, where autophagy is also required for synapse development, the synaptic assembly phenotype was not seen for *atg-4.1* or *atg-4.2* single-mutant animals but was evident in the *atg-4.1*; *atg-4.2* double-mutant animals (Figures S6C–S6G; Stavoe et al., 2016) and that the GFP::LGG-1 phenotype is enhanced in *atg-4.1; atg-4.2* double-mutant animals (Figures 4E, S6H, and S6I). Our results indicate that while *atg-4.1* and *atg-4.2* can act in a partially redundant fashion, they also display distinct phenotypes in LGG-1/LGG-2 puncta accumulation. Importantly, our findings indicate that *atg-4.2* is specifically necessary to prevent abnormal accumulation of autophagosomes in the neuronal soma.

ATG-4.2 Promotes Autophagosome Maturation

Our observations that lesions in *atg-4.2* result in animals with an abnormal accumulation of autophagosomes in the neuronal cell body are consistent with a model where *atg-4.2* acts late in the autophagy pathway to promote autophagosome maturation and autophagic degradation. Autophagosome maturation into an acidic autolysosome is mediated by fusion between autophagosomes and late endosomes or lysosomes in a process that requires the small GTPase Rab7 (Gutierrez et al., 2004; Hyttinen et al., 2013; Jäger et al., 2004). We reasoned that if *atg-4.2*-mutant animals have a defect at this step, then loss of *rab-7* function should phenocopy the *atg-4.2*-mutant phenotype.

Since null lesions in *rab-7* are lethal, we examined animals mutant for the *rab-7* activator *sand-1/Mon1* (Hegedűs et al., 2016; Poteryaev et al., 2007) and the *rab-7* effector, *epg-5* (Wang et al., 2016). We observed that indeed *sand-1*- and *epg-5*-mutant animals displayed increased autophagosome accumulation in the cell body compared to wild-type animals, similar to *atg-4.2(ola316)*-mutant animals (Figures 5A–5C and 5G). The observed phenotypes are specific to late blocks in autophagy, as mutant animals for genes involved in early events prior to autophagosome closure or trafficking, such as *atg-9(wy56)*, *atg-2(bp576)*, or *unc-16(ju146)*, did not display autophagosome accumulation in the cell body (Figure 5G). Also consistent with *atg-4.2* acting in a late step of autophagy to promote

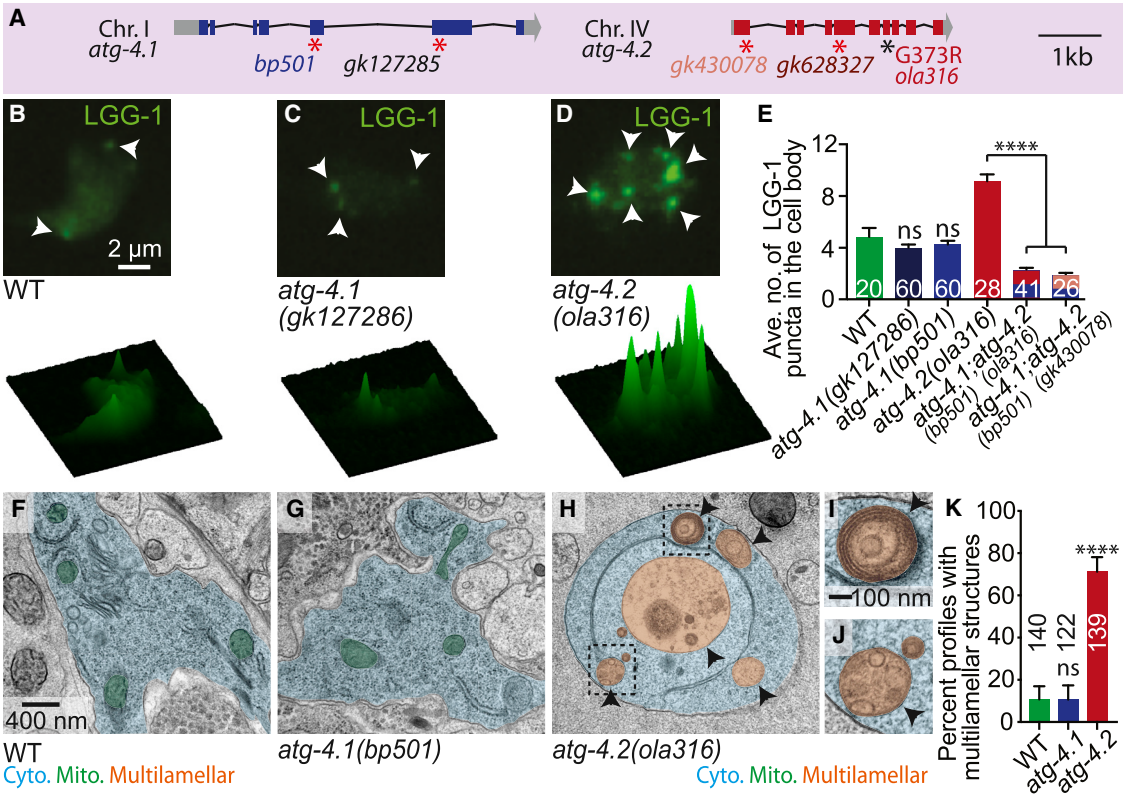

Figure 4. ATG-4.2, but Not ATG-4.1, Is Necessary for Clearance of Autophagosomes

(A) Schematic of the *atg-4.1* and *atg-4.2*-genomic regions on chromosomes I and IV, respectively, with exons (blue or red boxes), untranslated regions (gray boxes), and introns (black lines). Alleles affect indicated regions with early stop codons (red asterisks; *bp501* and *gk127285* in *atg-4.1* and *gk430078* and *gk628327* in *atg-4.2*) or amino acid changes (G373R for *ola316* in *atg-4.2*). Scale bar shows a 1-kb region.

(B–D) Autophagic vacuoles in the AIY cell body imaged as maximal projection of confocal z stacks (top row) and corresponding surface plots of the LGG-1 signal intensity (bottom row) in wild-type animals (B), *atg-4.1(gk127286)*-mutant animals (C), and *atg-4.2(ola316)*-mutant animals (D). Arrowheads denote LGG-1 puncta in the cell body.

(E) Quantification of the average number of LGG-1 puncta in the cell body of AIY in wild-type and indicated mutant and double-mutant animals. Error bars show standard error of the mean (SEM). ****$p < 0.0001$ by one-way ANOVA with Tukey's post hoc analysis between wild-type and mutant animals or as indicated. The numbers on the bars represent numbers of neurons examined; corresponding to $\geq$10 animals for each genotype. Abbreviations: ns, not significant (as compared to wild-type animals); AV, autophagic vacuole. Scoring was done by blindly quantifying maximal projections of confocal z stacks.

(F–H) Representative micrographs obtained by electron microscopy (EM) of neuronal cell bodies in wild-type animals (F), *atg-4.1(bp501)*-mutant animals (G), and *atg-4.2(ola316)*-mutant animals (H), with the cell bodies pseudo-colored in blue, mitochondria in green, and multilamellar autophagosome-like vacuoles in orange. See also Figure S5 for non-pseudo-colored images.

(I and J) Enlarged images of boxed areas showing multilamellar autophagosome-like vacuole examples from (H). See also Figure S5 for additional EM images.

(K) Quantification of the percentage of electron microscopy profiles with multilamellar autophagosome-like vacuoles in the cell somas of wild-type and mutant animals. Error bars show a 95% confidence interval. ****$p < 0.0001$ by Fisher's exact test between wild-type and mutant conditions. The numbers on the bars indicate the number of profiles scored; corresponding to $\geq$5 cell bodies from 2 different animals for each genotype. Abbreviations: ns, not significant (as compared to wild-type animals). Quantification was done by blindly scoring the electron micrograph somatic profiles.

Scale bar in (B) for (B)–(D); in (F) for (F)–(H), and in (I) for (I)–(J).

See also Figure S5.

autophagosome maturation, we found that *atg-4.2(gk628327); epg-5(tm3425)* double-mutant animals phenocopied either single mutant for the cell body accumulation phenotype, suggesting that they act in the same pathway in this process (Figure S6J). We do note however that the *atg-4.2(gk628327); epg-5(tm3425)* double-mutant animals also displayed an enhanced accumulation in the presynaptic region (Figure S6K), suggesting that they might perform distinct roles at presynaptic sites, which we did not further examine in this study. Together, our findings indicate that *atg-4.2*, similar to *sand-1* and *epg-5*, acts in a late stage of autophagy prior to degradation.

Atg-4.2 genetically interacts with *unc-16* in double-mutant animals to enhance the number of autophagosomes observed at the synapse. To test if *sand-1* also genetically interacts with *unc-16*, we created *sand-1(or552); unc-16(ju146)* double-mutant animals. We observed that similar to *atg-4.2; unc-16* double-mutant animals, *sand-1; unc-16* double-mutant animals also displayed dramatically enhanced accumulation of autophagosomes in the synaptic regions (Figures 5D–5F and 5H). Importantly, early autophagy mutants such as *atg-2* (required for autophagosome closure) (Velikkakath et al., 2012) and *atg-4.1* (required for LGG-1 priming) (Wu et al., 2012) failed to enhance

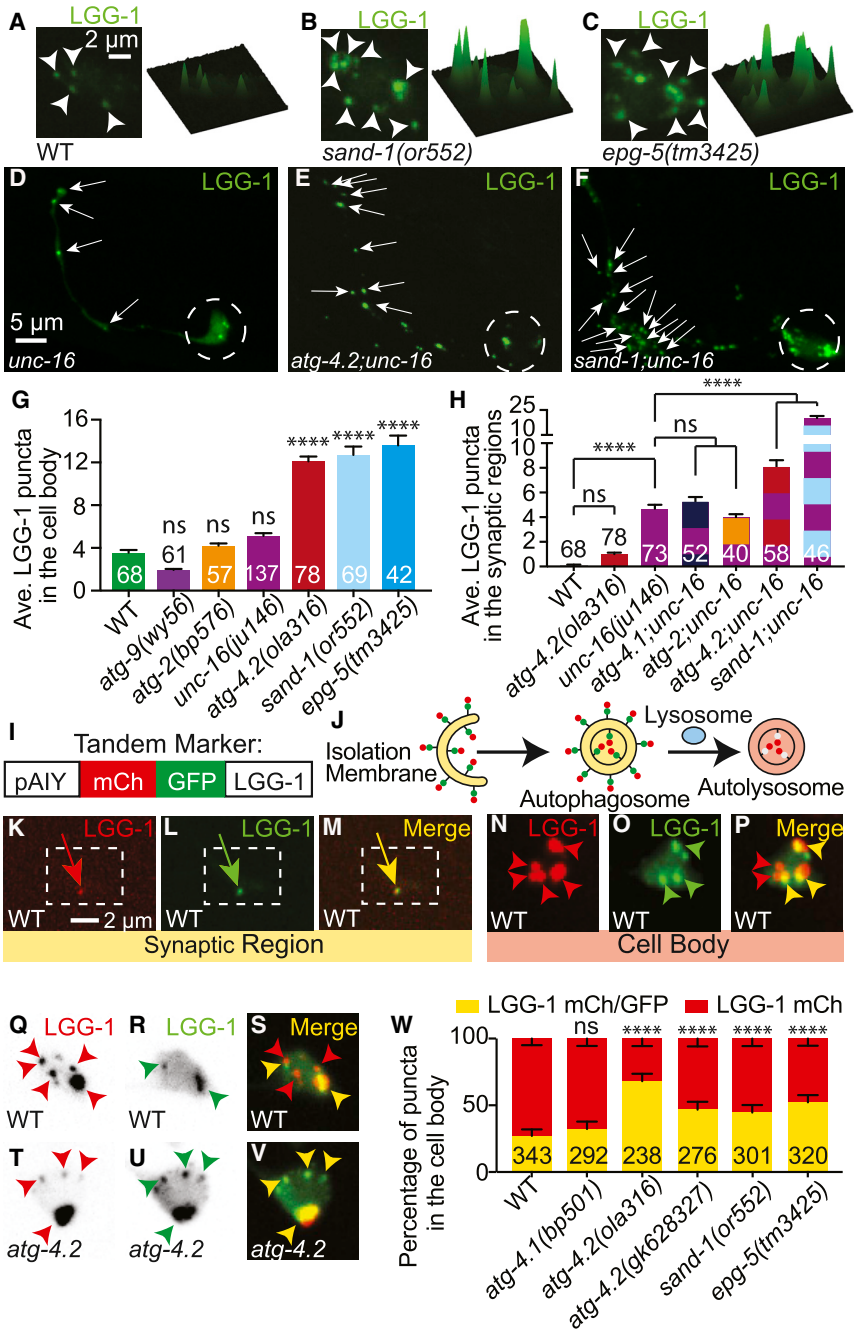

Figure 5. ATG-4.2 Promotes Autophagosome Maturation

(A–C) Autophagic vacuoles in the AIY cell body imaged as maximal projections of confocal z stacks (left) and corresponding surface plots of the LGG-1 signal intensity (right) in representative wild-type (A), *sand-1(or552)*-mutant (B), and *epg-5(tm3425)*-mutant (C) animals.

(D–F) Autophagic vacuoles (visualized with GFP::LGG-1) in representative *unc-16(ju146)*-mutant (D), *atg-4.2(ola316); unc-16(ju146)* double-mutant (E), and *sand-1(or552); unc-16(ju146)*double-mutant (F) neurons.

(G and H) Quantification of the average number of autophagic vacuoles in the cell body (G) or synaptic region (H) of AIY in wild-type and mutant or double-mutant animals. Alleles examined were *unc-16*(ju146), *atg-4.1(gk127286), atg-2(bp576), atg-4.2(ola316)*, *sand-1(or552),* or as indicated. Note that the increased severity of the *sand-1* enhancement might suggest a more complete block in autophagosome maturation than that of *atg-4.2*, which is partially redundant with *atg-4.1*. Error bars show standard error of the mean (SEM). ***p < 0.001; ****p < 0.0001 by one-way ANOVA with Tukey's post hoc analysis between wild-type and mutant animals or as indicated. The numbers on the bars represent number of neurons examined. Abbreviations: ns, not significant (as compared to wild-type animals); AV, autophagic vacuole.

(I and J) Schematic for the tandem LGG-1 marker (mCh::GFP::LGG-1) showing the construct configuration with the AIY promoter (I) and the progression of the tandem LGG-1 marker through the stages of autophagosome biogenesis, fusion with lysosomes, and acidification (J) (Chang et al., 2017; Kimura et al., 2007).

(K–P) Autophagic vacuoles in a representative wild-type AIY neuron, visualized with the tandem marker (mCh::GFP::LGG-1) in the synaptic region (K–M) and the cell body (N–P). The mCherry channel (K and N), GFP channel (L and O), and merge (M and P) are shown separately. In (K)–(M), the dashed box encloses the synapse-rich portion of the synaptic region (similar to Figure 1A–1D).

(Q–V) Autophagic vacuoles in representative wild-type (Q–S) and *atg-4.2(ola316)*-mutant (T–V) cell bodies, visualized with the tandem marker (mCh::GFP::LGG-1). The mCherry channel (Q and T), GFP channel (R and U), and merge (S and V) are shown separately. Single channels (Q, R, T, and U) are inverted to better show dim red puncta.

(W) Quantification of puncta labeled with the LGG-1 tandem marker in the cell body, showing the percentage of puncta with mCh-and-GFP-colocalized signal (yellow, immature) or mCh-only signal (mature). Error bars show a 95% confidence interval. **** p < 0.0001 by Fisher's exact test between wild-type and mutant animals. The numbers on the bars indicate the number of puncta scored, corresponding to ≥27 neurons for each genotype. Abbreviations: ns, not significant (as compared to wild-type animals).

Arrowheads denote LGG-1 puncta in the cell body. Arrows denote LGG-1 puncta in the synaptic regions. Dashed circles enclose cell bodies. In merge images (M, P, S, and V), red arrowheads refer to puncta labeled with only mCh (representing acidified autophagic vacuoles), while yellow arrows and arrowheads refer to structures labeled with both mCh and GFP (representing autophagosomes that have not yet been acidified). Quantifications were done by blindly scoring maximal projections of confocal micrographs.

Scale bar(s) in (A) for (A)–(C) and (N)–(V); in (D) for (D)–(F); in (K) for (K)–(M).

See also Figure S6.

the neurite accumulation phenotype observed in *unc-16*-mutant animals (Figure 5H). Our findings indicate that the observed enhancement of *unc-16* with either *sand-1* or *atg-4.2* is a specific phenotype resulting from a genetic interaction between defects in retrograde transport and defects in autophagosome degradation.

We then tested the acidification state of autophagic vacuoles by employing a tandem label strategy in which LGG-1 was fused to both mCherry and GFP (Figure 5I; lipidation controls in Figures S7A–S7D; Chang et al., 2017; Kimura et al., 2007). Briefly, in this strategy, immature autophagosomes are labeled with both GFP and mCherry, but because GFP is preferentially quenched in acidic environments, autophagic structures lose their GFP signal and display solely mCherry signal when mature (schematic, Figure 5J). Comparisons with the tandem marker lipidation control (Figures S7A–S7D), suggest that while structures positive for both GFP and mCh are lipidated, some structures positive for mCh, but negative for GFP accumulate in acidified lysosomes (see Figure S7 and STAR Methods). Using this approach *in vivo* and in single neurons of wild-type animals, we observed that 88% of synaptic LGG-1-labeled structures were positive for mCh and GFP signal (Figures 5K–5M and S7H). In contrast, examination of LGG-1-labeled structures in the cell-body region of the neurons demonstrated that over 70% of the structures were positive for mCherry but not for GFP (Figures 5N–5P). Our findings in wild-type animals are consistent with studies that demonstrate that active lysosomes are preferentially enriched in the neuronal cell soma (Hollenbeck, 1993; Kaasinen et al., 2008) and suggest that most autophagosomes at synapses mature as they are transported to the neuronal cell body.

To better understand the ability of the tandem marker to assess the maturation state of autophagosomes in mutant animals, we first examined it in *sand-1/Mon1* (Hegedűs et al., 2016; Poteryaev et al., 2007) and *epg-5* (Wang et al., 2016) mutant animals, which are known to block autophagosome acidification. We observed that compared to wild-type animals, the percentage of mature LGG-1 structures (mCh positive, GFP negative) decreases (Figure 5W), as expected given the known mechanism of action of these genes in autophagosome maturation.

We then used the tandem marker to examine the maturation state of autophagosomes in *atg-4.2*- mutant animals. For two independent alleles of *atg-4.2*, we observed that a higher percentage of autophagic vacuoles were immature (positive for both GFP and mCh signal) compared to wild-type or *atg-4.1*-mutant animals (Figures 5Q–5W). The immature state of the autophagic puncta in *atg-4.2*-mutant animals could be a result of the failure to remove LGG-1 from the outside of the autophagosome (where it would not be acidified), failure to undergo internal acidification, or both, possibilities that would need to be further distinguished through biochemical assays (see below). Nevertheless, these findings with the tandem marker indicate that *atg-4.2*, but not *atg-4.1*, is required for late stages in the progression of autophagy.

ATG-4.2 Delipidates LGG-1 and Is Necessary for the Formation of Autolysosomes that Degrade Synaptic Proteins

Why is *atg-4.2*, but not *atg-4.1*, required for the late stages of autophagy? Atg4s are cysteine proteases that cleave Atg8/GABARAP/LC3/LGG-1/LGG-2 to (1) activate LGG-1 for conjugation onto the autophagosomal membrane (early event) or (2) remove LGG-1/LGG-2 from the autophagosomal membrane (late event) (Kirisako et al., 2000; Maruyama and Noda, 2017; Figure 6A). We wondered if ATG-4.2 might have distinct biochemical activity toward LGG-1 in these steps.

We tested ATG-4.2 activity on LGG-1 by generating recombinant *C. elegans* ATG-4.2, and in a biochemically reconstituted system examining either (1) ATG-4.2 priming activity on the C-terminal of LGG-1 using a construct with an extended C terminus (LGG-1-His), or (2) delipidation activity on LGG-1 conjugated onto liposomes as described by Kauffman et al. (2018). We observed that after 8 min, 89% of liposomal LGG-1 was cleaved, but only 18% of LGG-1-His was cleaved (average of three independent experiments; Figure 6B), indicating that ATG-4.2 preferentially delipidates (or removes) LGG-1 from autophagosomal membranes. Our biochemical results are consistent with our cell biological and genetic data and together suggest a model whereby delipidation of LGG-1, specifically by ATG-4.2, is a necessary step for correct maturation of autophagosomes.

To gain further insights into the effects of ATG-4.2 on autophagic progression, we examined if there were defects in the autolysosomes of *atg-4.2*-mutant animals. Formation of autolysosomes, which occurs through the fusion of autophagosomes and lysosomes, is a necessary step in autophagosome maturation and can be assayed by probing the colocalization of lysosomal proteins, such as LAAT-1 (Liu et al., 2012) and the autophagy protein LGG-1 (Hyttinen et al., 2013; Maday et al., 2012; Zhang et al., 2015). We observed that in wild-type animals, 91% of the LGG-1 puncta in the cell body colocalized with LAAT-1 (Figures S7I–S7P), consistent with a progression toward autophagosomes-lysosome fusion and acidification as autophagic structures are transported toward the neuronal cell body. In *atg-4.2*-mutant animals, while there was no change in LGG-1/LAAT-1 colocalization in the synaptic region, nor in the total number of LGG-1 and/or LAAT-1 structures in the cell body (Figures S7I and S7Q), there was a significant reduction in colocalization of LGG-1 and LAAT-1 (Figures 6C–6E). These findings are consistent with a role for *atg-4.2* in promoting autolysosome formation in the neuronal cell body.

Next, we examined the maturation state of the autolysosomes by using the LGG-1 tandem marker while simultaneously visualizing LAAT-1:BFP. Consistent with our previous findings, we observed that in wild-type animals, 92% of LAAT-1 and LGG-1 colocalized structures were mature (red positive, green negative), while in *atg-4.2(ola316)*-mutant animals, only 33% of LAAT-1 and LGG-1 colocalized structures were mature (Figures 6F–6H). This effect was, at least in part, due to a failure to delipidate LGG-1 from the cytoplasmic face of the autolysosomes but might also reflect a defect in internal acidification. Our observations are consistent with *atg-4.2*-mutant animals having a defect in the maturation of autophagic structures and suggest that ATG-4.2 is necessary for the formation of autolysosomes.

To examine how *atg-4.2* affects the acidification of autophagic cargo, we visualized the colocalization of synaptic proteins with LGG-1 in the neuronal cell body. Consistent with the role of autophagy in degrading synaptic material and with the role of ATG-4.2 in the clearance of autophagic structures, we observed that *atg-4.2*-mutant animals displayed an increased percentage of autophagosomes colocalized with synaptic proteins in the cell soma (Figures 6I–6K and S7R). Moreover, generation of a synaptic tandem marker, which enabled visualization of the internal acidification state of compartments containing synaptic material, revealed that in *atg-4.2*-mutant animals there were fewer compartments in which synaptic proteins were acidified

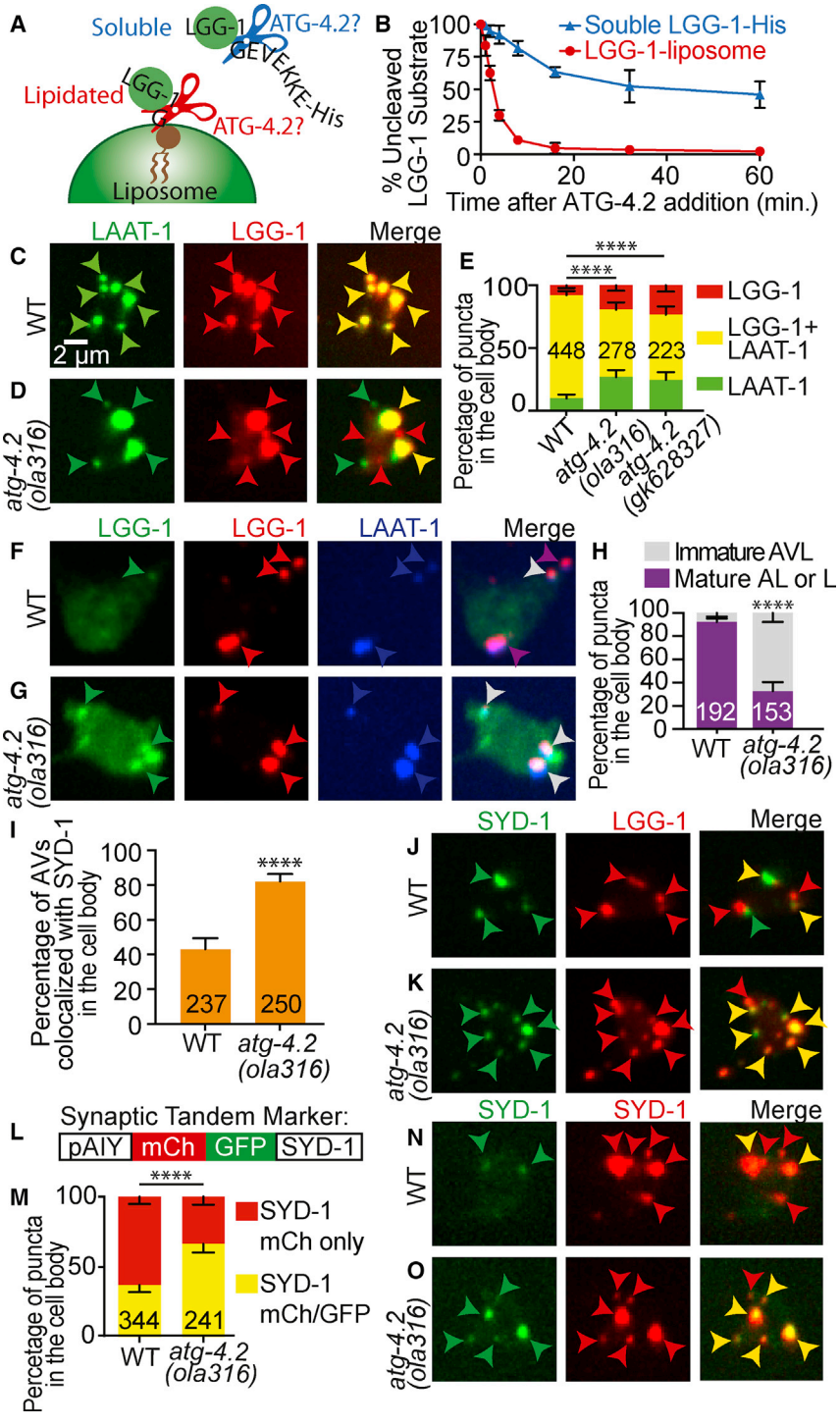

Figure 6. ATG-4.2 Delipidates LGG-1 to Promote Formation and Acidification of Autolysosomes and Breakdown of Synaptic Cargo

(A and B) Biochemical characterization of ATG-4.2 activity. Cartoon diagram displaying the tested conditions in the reconstituted biochemical system: cleavage of a soluble LGG-1 substrate (LGG1-His) mimicking priming (blue), which precedes lipidation onto autophagosomal membranes, or cleavage of lipidated LGG-1 on liposomes, mimicking release from the autophagic membrane, delipidation (red). In (B), error bars show the standard deviation of three independent experiments.

(C–E) Lysosomes (LAAT-1::GFP, green arrowheads), autophagosomes (mCh::LGG-1, red arrowheads), and autolysosomes (colocalization of LAAT-1 and LGG-1, yellow arrowheads in merge images) are visualized in the AIY cell body of wild-type (C) and *atg-4.2(ola316)*-mutant animals (D). In (E), quantification of the percentage of puncta in the cell body displaying LAAT-1::GFP, mCh::LGG-1 or colocalization of these two markers in the indicated genotypes is shown. Error bars show a 95% confidence interval. ****$p < 0.0001$ by chi-square test between wild-type and mutant animals. The numbers on the bars indicate the number of puncta scored, corresponding to ≥66 neurons for each genotype.

(F–H) Autophagic vacuoles visualized with the tandem marker (mCh::GFP::LGG-1) and lysosomes visualized with LAAT-1:BFP in the AIY cell body of wild-type animals (F) and *atg-4.2(ola316)*-mutant animals (G). In merge images, gray arrowheads refer to immature autolysosomes (AVL) (positive for mCh, GFP, and BFP) while purple arrowheads refer to mature autolysosomes (AL) (or mature lysosomes, represented as L in legend) (positive for mCh and BFP). In (H), quantification of the percentage of puncta in the cell bodies that represent either mature or immature autolysosomes based on the tandem marker analyses is shown. Error bars show a 95% confidence interval. ****$p < 0.0001$ by Fisher's exact test between wild-type and mutant animals. The numbers on the bars indicate the number of puncta scored, corresponding to ≥39 neurons for each genotype.

(I–K) Quantification of the percentage of autophagic vacuoles (mCh::LGG-1) displaying colocalization with the presynaptic protein GFP::SYD-1 in the cell body of AIY interneurons (I). Error bars show a 95% confidence interval. ****$p < 0.0001$ by Fisher's exact test between wild-type and mutant animals. The numbers on the bars indicate the number of puncta scored, corresponding to ≥50 neurons for each genotype. Abbreviations: AVs, autophagic vacuoles. In (J)–(K), representative confocal micrographs of the colocalization of presynaptic active zone protein GFP::SYD-1 (first column in J and K), mCh::LGG-1 (second column in J and K), and merge images (third column in J and K) in wild-type animals (J) and *atg-4.2(ola316)*-mutant animals (K). In merge images, green arrowheads refer to accumulation of SYD-1, red arrowheads to LGG-1 puncta, and yellow arrowheads to colocalization of LGG-1 and SYD-1, indicative of autophagic vacuoles with synaptic material.

(L–O) Schematic for the tandem SYD-1 active zone protein marker (mCh::GFP::SYD-1) showing the construct configuration with the AIY promoter (L). Quantification of the percentage of SYD-1 puncta displaying mCh only (representing SYD-1 in an acidified compartment), or mCh and GFP (representing SYD-1 in an environment that is not acidified) (M). Error bars show a 95% confidence interval. ****$p < 0.0001$ by Fisher's exact test between wild-type and mutant animals. The numbers on the bars indicate the number of puncta scored, corresponding to ≥46 neurons for each genotype. In (N) and (O), representative confocal images of the tandem SYD-1 presynaptic active zone protein marker in wild-type animals (N) and *atg-4.2(ola316)*-mutant animals (O) are shown. In merge images, red

(legend continued on next page)

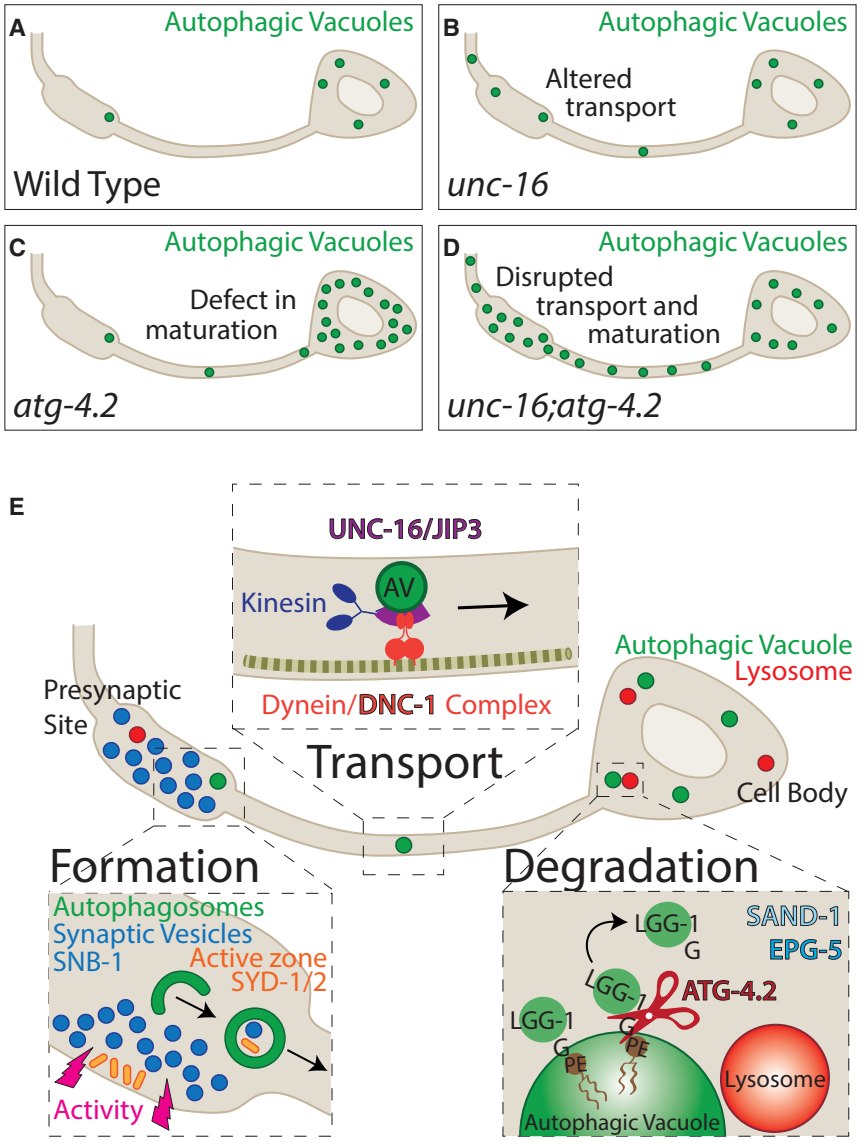

Figure 7. Synaptic Autophagy: A Model from Birth at the Synapse to Breakdown in the Cell Body

(A–D) Schematics of autophagic vacuole localization in wild-type (A), *unc-16*-mutant (B), *atg-4.2*-mutant (C), and *unc-16; atg-4.2* double-mutant animals (D). Disruption of retrograde transport (*unc-16* mutant) or maturation (*atg-4.2* mutant) leads to autophagosome accumulation in the neurite or the cell body, respectively, and these pathways cooperate to clear autophagosomes from the synapse (D).

(E) Model schematic illustrating the steps of synaptic autophagy in the neuron, and the key molecules involved. Formation: autophagosomes form at presynaptic sites, influenced by the state of synaptic activity of the neuron (Figure 1; Shehata et al., 2012; Soukup et al., 2016; Wang et al., 2015) through ordered transport and assembly of autophagy molecules (Maday and Holzbaur, 2014), including ATG-9 (Stavoe et al., 2016). Synaptic autophagosomes contain post-synaptic proteins, synaptic vesicles (Nikoletopoulou et al., 2017; Okerlund et al., 2017; Rowland et al., 2006), and active zone proteins. Transport: autophagosomes undergo retrograde transport toward the cell body, a process dependent on the dynein activator dynactin/DNC-1 and the motor adaptor UNC-16/JIP3. Degradation: once in the cell body, the autophagy protease ATG-4.2 cleaves LGG-1 and LGG-2 off the autophagic vacuole membrane to facilitate maturation and degradation in a process that also requires the RAB-7 activator SAND-1/Mon1 and effector EPG-5.

(Figures 6L–6O). Together, our findings indicate that *atg-4.2*-mutant animals are defective in acidification, resulting in an accumulation of immature autophagosomes with undigested cargo including synaptic material.

DISCUSSION

Distinct steps of the autophagy pathway occur in different subcellular compartments. *In vivo*, autophagosome biogenesis occurs at presynaptic sites (Soukup et al., 2016; Stavoe et al., 2016) and the number of autophagosomes in the neurite can be increased by stimulating the activity of neurons (Figure 1; Shehata et al., 2012; Soukup et al., 2016; Wang et al., 2015). Autophagosomes then undergo retrograde trafficking prior to degradation (Maday et al., 2012), indicating a regional decoupling of biogenesis and degradation. In this study, we extend these observations by demonstrating that in *C. elegans*, the number of synaptic autophagosomes in the AIY interneuron predictably changed depending on the firing state of the neuron, which we could manipulate by altering physiological stimuli that promote AIY responses, by genetically inhibiting synaptic transmission or by chemo-genetically altering the response state of the neuron. We also observed colocalization of synaptic proteins with autophagosomes in the cell body, further indicating a link between autophagosome biogenesis at the synapse and autophagy-mediated degradation of synaptic proteins in the soma. Our findings extend our understanding of autophagy regulation in neurons and uncover mechanisms linking autophagosomes at the synapse with their clearance in the cell soma.

UNC-16/JIP3-dependent retrograde transport plays an important role in transport and clearance of synaptic

arrowheads refer to active zone protein SYD-1 puncta labeled with only mCh, while yellow arrowheads refer to structures labeled with both mCh and GFP.
In (E), (H), (I), and (M), quantifications were done by blindly scoring maximal projections of confocal micrographs.
Scale bar in (C) for (C), (D), (F), (G), (J), (K), (N), and (O).
See also Figure S7.

autophagosomes. In *C. elegans*, *Drosophila*, and vertebrate neurons, axonal autophagosomes are transported toward the cell body via the dynein complex (Cheng et al., 2015; Ikenaka et al., 2013; Katsumata et al., 2010; Neisch et al., 2017). UNC-16/JIP3/Sunday Driver, a motor adaptor protein that interacts with dynein, plays important and conserved roles in the regulated localization and transport of late endosomes and lysosomes, as well as other organelles (Brown et al., 2009; Byrd et al., 2001; Drerup and Nechiporuk, 2013; Edwards et al., 2013, 2015;; Gowrishankar et al., 2017). Our findings now demonstrate that UNC-16/JIP3 is also required for autophagosome retrograde transport. In vertebrate neurons, autophagosome retrograde transport is promoted by JIP1, a motor adaptor protein that belongs to the same family as UNC-16/JIP3 (Fu and Holzbaur, 2014; Fu et al., 2014). While we did not detect a phenotype for autophagosome retrograde transport in an available *C. elegans jip-1* nonsense allele (for which partial function is unknown), we note that JIP1 and JIP3 share sequence and functional similarities and are also known to cooperate in the transport of cargo (Hammond et al., 2008; Sun et al., 2017). Together, our findings ascribe an important and potentially conserved role for UNC-16/JIP3 in retrograde transport of autophagosomes in *C. elegans* neurons.

Impaired retrograde transport in *unc-16/jip3*-mutant animals resulted in accumulation of LGG-1-containing structures in the neurites. In vertebrate neurons, disruption of retrograde transport also causes accumulation of autophagosomes and lysosomes in swollen neuronal processes and synapses. This, in turn, results in autophagic stress and in neurodegeneration phenotypes similar to those seen in the neurons of Alzheimer's disease patients (Ikenaka et al., 2013; Lee et al., 2011; Nixon et al., 2005; Takáts et al., 2013). Specific disruption of JIP3 in vertebrate neurons has also been associated with an increase in soluble Aβ levels, plaque size, plaque abundance, and axonal dystrophy (Gowrishankar et al., 2017). Our findings in *C. elegans* neurons are consistent with these studies and underscore the importance of retrograde transport in linking the mechanisms of autophagosome biogenesis at the synapse with degradation in the cell body. Furthermore, our observations that combined defects in both retrograde transport and degradation machinery enhanced autophagosome accumulation in the neurites raises the question of whether the accumulated autophagosomes seen in progressive neurodegenerative diseases might result from an accruement of specific dysfunctions in transport and clearance of autophagosomes.

ATG-4.2 genetically cooperates with UNC-16/JIP3 in the clearance of autophagic vacuoles from axons (Figures 7A–7D). ATG-4.2 is one of two Atg4 cysteine proteases in *C. elegans* (Wu et al., 2012). Atg4 cysteine proteases are required during both early and late stages of autophagy to cleave Atg8/LGG-1/LGG-2 but to achieve two distinct functions: the first cleavage (priming) is required for the conjugation of LGG-1 to the autophagosomal membrane to promote autophagosome elongation during biogenesis, while the second cleavage (delipidation) removes LGG-1/LGG-2 from the membrane prior to autophagic degradation (Kirisako et al., 2000; Maruyama and Noda, 2017). Our biochemical and cell biological studies indicate that ATG-4.2 preferentially performs delipidation on LGG-1 to remove it from autophagic membranes and that this step is necessary for the fusion of autophagosomes with lysosomes and degradation.

Our findings, together with previous *in vitro* studies showing that ATG-4.1 is the dominant priming protease (Wu et al., 2012), are consistent with a model whereby distinct cleavage roles in LGG-1/Atg8 priming and delipidation might be regulated *in vivo* by distinct ATG4 proteases. In support of this idea, a recent biochemical study examining mammalian ATG4 proteins revealed that different ATG4s possess different activities for cleaving soluble or membrane-bound GABARAP/Atg8/LGG-1 (Kauffman et al., 2018). Distinct ATG4 proteases could therefore modulate the association of LGG-1/LGG-2 with autophagic membranes either during priming or delipidation, and these regulated steps could "bookend" the progression of autophagy from biogenesis to degradation (model presented in Figure 7E). Disruption of retrograde transport of synaptic autophagosomes, or defective delipidation of LGG-1/LGG-2 by ATG-4.2, would enhance abnormal accumulation of autophagosomes in neurons and result in cell biological phenotypes reminiscent to those seen in neurodegenerative diseases.

STAR★METHODS

Detailed methods are provided in the online version of this paper and include the following:

- KEY RESOURCES TABLE
- CONTACT FOR REAGENT AND RESOURCE SHARING
- EXPERIMENTAL MODEL AND SUBJECT DETAILS
  - *C. elegans* Strains and Genetics
  - Molecular Biology and Transgenic Lines
- METHOD DETAILS
  - Fluorescence Microscopy and Confocal Imaging
  - SNP Mapping and Whole-Genome Sequencing
  - Electron Microscopy
  - Purification of *C. elegans* Proteins
  - Proteoliposome Preparation
  - *In Vitro* Proteolysis Assays
- QUANTIFICATION AND STATISTICAL ANALYSIS
  - Quantification of Autophagosomes in AIY
  - Activity-dependent Autophagy
  - AV Accumulation in Neurites and Cell Bodies
  - Autophagosome Dynamics
  - Tandem Markers and Colocalization Assays
  - Other Quantifications in AIY
  - Statistical Analyses

SUPPLEMENTAL INFORMATION

Supplemental Information can be found with this article online at https://doi.org/10.1016/j.devcel.2019.02.013.

ACKNOWLEDGMENTS

We thank members of the Colón-Ramos lab, Melia lab, Shawn Ferguson (Yale University), and Andrea Stavoe (University of Pennsylvania) for their thoughtful comments. We thank Enrique Cruz-Reyes (Universidad de Puerto Rico, Cayey), Alec Rodriguez, Sisi Yang, and Joon Lee (Colón-Ramos lab) for experimental assistance. We thank the Caenorhabditis Genetics Center (supported by NIH P40 OD010440), the Mitani laboratory (Tokyo Women's Medical University), and the Hong Zhang laboratory (Institute of Biophysics, Chinese

Academy of Sciences) for strains. We thank Z. Altun (www.wormatlas.org) for diagrams used in the figures. We thank the Research Center for Minority Institutions program, the Marine Biological Laboratories (MBL), and the Instituto de Neurobiología de la Universidad de Puerto Rico for providing meeting and brainstorming platforms. This work made use of the BioCryo facility of Northwestern University's NUANCE Center (supported by NSF ECCS-1542205; NSF DMR-1720139; and the International Institute for Nanotechnology by the State of Illinois); and the CryoCluster equipment (funded by NSF DMR-1229693). Images were acquired using instruments in the Electron Microscopy Core of UIC's Research Resources Center. Support for T.J.M. was provided by NIH grant (GM1000930), and support for K.J.K. and S.E.H. was provided by T32-GM007223. S.E.H. was also supported by NSF GRF DGE-1122492. Research in the DACR lab was supported by NSF IOS 1353845, NIH R01NS076558, and an HHMI Scholar Award.

AUTHOR CONTRIBUTIONS

S.E.H. and D.A.C.-R. designed the experiments. S.E.H. performed the experiments and data analyses. K.J.K. and T.J.M. performed the protein purifications, biochemical assays, and corresponding data analysis. M.K. and J.E.R. performed the electron microscopy experiments and analyzed the data. S.E.H. and D.A.C.-R. prepared the manuscript.

DECLARATION OF INTERESTS

The authors declare no competing interests.

Received: March 10, 2018
Revised: December 17, 2018
Accepted: February 12, 2019
Published: March 14, 2019

REFERENCES

Abe, Y., Shodai, T., Muto, T., Mihara, K., Torii, H., Nishikawa, S., Endo, T., and Kohda, D. (2000). Structural basis of presequence recognition by the mitochondrial protein import receptor Tom20. Cell *100*, 551–560.

Alberti, A., Michelet, X., Djeddi, A., and Legouis, R. (2010). The autophagosomal protein LGG-2 acts synergistically with LGG-1 in Dauer formation and longevity in C. elegans. Autophagy *6*, 622–633.

Arimoto, M., Koushika, S.P., Choudhary, B.C., Li, C., Matsumoto, K., and Hisamoto, N. (2011). The Caenorhabditis elegans JIP3 protein UNC-16 functions as an adaptor to link kinesin-1 with cytoplasmic dynein. J. Neurosci. *31*, 2216–2224.

Baas, P.W., and Lin, S. (2011). Hooks and comets: the story of microtubule polarity orientation in the neuron. Dev. Neurobiol. *71*, 403–418.

Biron, D., Shibuya, M., Gabel, C., Wasserman, S.M., Clark, D.A., Brown, A., Sengupta, P., and Samuel, A.D. (2006). A diacylglycerol kinase modulates long-term thermotactic behavioral plasticity in C. elegans. Nat. Neurosci. *9*, 1499–1505.

Borland, H., and Vilhardt, F. (2017). Prelysosomal compartments in the unconventional secretion of amyloidogenic seeds. Int. J. Mol. Sci. *18*, https://doi.org/10.3390/ijms18010227.

Brown, H.M., Van Epps, H.A., Goncharov, A., Grant, B.D., and Jin, Y. (2009). The JIP3 scaffold protein UNC-16 regulates RAB-5 dependent membrane trafficking at C. elegans synapses. Dev. Neurobiol. *69*, 174–190.

Byerly, L., Cassada, R.C., and Russell, R.L. (1976). The life cycle of the nematode Caenorhabditis elegans. I. Wild-type growth and reproduction. Dev. Biol. *51*, 23–33.

Byrd, D.T., Kawasaki, M., Walcoff, M., Hisamoto, N., Matsumoto, K., and Jin, Y. (2001). UNC-16, a JNK-signaling scaffold protein, regulates vesicle transport in C. elegans. Neuron *32*, 787–800.

Cavalli, V., Kujala, P., Klumperman, J., and Goldstein, L.S. (2005). Sunday Driver links axonal transport to damage signaling. J. Cell Biol. *168*, 775–787.

Chai, Y., Li, W., Feng, G., Yang, Y., Wang, X., and Ou, G. (2012). Live imaging of cellular dynamics during Caenorhabditis elegans postembryonic development. Nat. Protoc. *7*, 2090–2102.

Chang, J.T., Kumsta, C., Hellman, A.B., Adams, L.M., and Hansen, M. (2017). Spatiotemporal regulation of autophagy during Caenorhabditis elegans aging. Elife *6*.

Cheng, X.T., Zhou, B., Lin, M.Y., Cai, Q., and Sheng, Z.H. (2015). Axonal autophagosomes recruit dynein for retrograde transport through fusion with late endosomes. J. Cell Biol. *209*, 377–386.

Choy, A., Dancourt, J., Mugo, B., O'Connor, T.J., Isberg, R.R., Melia, T.J., and Roy, C.R. (2012). The Legionella effector RavZ inhibits host autophagy through irreversible Atg8 deconjugation. Science *338*, 1072–1076.

Clark, D.A., Biron, D., Sengupta, P., and Samuel, A.D. (2006). The AFD sensory neurons encode multiple functions underlying thermotactic behavior in Caenorhabditis elegans. J. Neurosci. *26*, 7444–7451.

Colón-Ramos, D.A., Margeta, M.A., and Shen, K. (2007). Glia promote local synaptogenesis through UNC-6 (netrin) signaling in C. elegans. Science *318*, 103–106.

Davis, M.W., and Hammarlund, M. (2006). Single-nucleotide polymorphism mapping. Methods Mol. Biol. *351*, 75–92.

Davis, M.W., Hammarlund, M., Harrach, T., Hullett, P., Olsen, S., and Jorgensen, E.M. (2005). Rapid single nucleotide polymorphism mapping in C. elegans. BMC Genomics *6*, 118.

Dittman, J.S., and Kaplan, J.M. (2006). Factors regulating the abundance and localization of synaptobrevin in the plasma membrane. Proc. Natl. Acad. Sci. USA *103*, 11399–11404.

Drerup, C.M., and Nechiporuk, A.V. (2013). JNK-interacting protein 3 mediates the retrograde transport of activated c-Jun N-terminal kinase and lysosomes. PLoS Genet. *9*, e1003303.

Edwards, S.L., Morrison, L.M., Yorks, R.M., Hoover, C.M., Boominathan, S., and Miller, K.G. (2015). UNC-16 (JIP3) acts through synapse-assembly proteins to inhibit the active transport of cell soma organelles to Caenorhabditis elegans motor neuron axons. Genetics *201*, 117–141.

Edwards, S.L., Yu, S.C., Hoover, C.M., Phillips, B.C., Richmond, J.E., and Miller, K.G. (2013). An organelle gatekeeper function for Caenorhabditis elegans UNC-16 (JIP3) at the axon initial segment. Genetics *194*, 143–161.

Fu, M.M., and Holzbaur, E.L. (2014). Integrated regulation of motor-driven organelle transport by scaffolding proteins. Trends Cell Biol. *24*, 564–574.

Fu, M.M., Nirschl, J.J., and Holzbaur, E.L.F. (2014). LC3 binding to the scaffolding protein JIP1 regulates processive dynein-driven transport of autophagosomes. Dev. Cell *29*, 577–590.

Gowrishankar, S., Wu, Y., and Ferguson, S.M. (2017). Impaired JIP3-dependent axonal lysosome transport promotes amyloid plaque pathology. J. Cell Biol. *216*, 3291–3305.

Gutierrez, M.G., Munafó, D.B., Berón, W., and Colombo, M.I. (2004). Rab7 is required for the normal progression of the autophagic pathway in mammalian cells. J. Cell Sci. *117*, 2687–2697.

Hammond, J.W., Griffin, K., Jih, G.T., Stuckey, J., and Verhey, K.J. (2008). Co-operative versus independent transport of different cargoes by Kinesin-1. Traffic *9*, 725–741.

Han, L., Zhao, Y., Zhang, X., Peng, J., Xu, P., Huan, S., and Zhang, M. (2014). RFP tags for labeling secretory pathway proteins. Biochem. Biophys. Res. Commun. *447*, 508–512.

Hawk, J.D., Calvo, A.C., Liu, P., Almoril-Porras, A., Aljobeh, A., Torruella-Suárez, M.L., Ren, I., Cook, N., Greenwood, J., Luo, L., et al. (2018). Integration of plasticity mechanisms within a single sensory neuron of C. elegans actuates a memory. Neuron *97*, 356–367.

Hegedűs, K., Takáts, S., Boda, A., Jipa, A., Nagy, P., Varga, K., Kovács, A.L., and Juhász, G. (2016). The Ccz1-Mon1-Rab7 module and Rab5 control distinct steps of autophagy. Mol. Biol. Cell *27*, 3132–3142.

Hollenbeck, P.J. (1993). Products of endocytosis and autophagy are retrieved from axons by regulated retrograde organelle transport. J. Cell Biol. *121*, 305–315.

Horenkamp, F.A., Kauffman, K.J., Kohler, L.J., Sherwood, R.K., Krueger, K.P., Shteyn, V., Roy, C.R., Melia, T.J., and Reinisch, K.M. (2015). The Legionella anti-autophagy effector RavZ targets the autophagosome via PI3P- and curvature-sensing motifs. Dev. Cell *34*, 569–576.

Hosono, R., Mitsui, Y., Sato, Y., Aizawa, S., and Miwa, J. (1982). Life span of the wild and mutant nematode Caenorhabditis elegans. Effects of sex, sterilization, and temperature. Exp. Gerontol. *17*, 163–172.

Hyttinen, J.M., Niittykoski, M., Salminen, A., and Kaarniranta, K. (2013). Maturation of autophagosomes and endosomes: a key role for Rab7. Biochim. Biophys. Acta *1833*, 503–510.

Ikenaka, K., Kawai, K., Katsuno, M., Huang, Z., Jiang, Y.M., Iguchi, Y., Kobayashi, K., Kimata, T., Waza, M., Tanaka, F., et al. (2013). dnc-1/dynactin 1 knockdown disrupts transport of autophagosomes and induces motor neuron degeneration. PLoS One *8*, e54511.

Itakura, E., Kishi-Itakura, C., and Mizushima, N. (2012). The hairpin-type tail-anchored SNARE syntaxin 17 targets to autophagosomes for fusion with endosomes/lysosomes. Cell *151*, 1256–1269.

Jäger, S., Bucci, C., Tanida, I., Ueno, T., Kominami, E., Saftig, P., and Eskelinen, E.L. (2004). Role for Rab7 in maturation of late autophagic vacuoles. J. Cell Sci. *117*, 4837–4848.

Kaasinen, S.K., Harvey, L., Reynolds, A.J., and Hendry, I.A. (2008). Autophagy generates retrogradely transported organelles: a hypothesis. Int. J. Dev. Neurosci. *26*, 625–634.

Katayama, H., Yamamoto, A., Mizushima, N., Yoshimori, T., and Miyawaki, A. (2008). GFP-like proteins stably accumulate in lysosomes. Cell Struct. Funct. *33*, 1–12.

Katsumata, K., Nishiyama, J., Inoue, T., Mizushima, N., Takeda, J., and Yuzaki, M. (2010). Dynein- and activity-dependent retrograde transport of autophagosomes in neuronal axons. Autophagy *6*, 378–385.

Kauffman, K.J., Yu, S., Jin, J., Mugo, B., Nguyen, N., O'Brien, A., Nag, S., Lystad, A.H., and Melia, T.J. (2018). Delipidation of mammalian Atg8-family proteins by each of the four ATG4 proteases. Autophagy *14*, 992–1010.

Kimura, S., Noda, T., and Yoshimori, T. (2007). Dissection of the autophagosome maturation process by a novel reporter protein, tandem fluorescent-tagged LC3. Autophagy *3*, 452–460.

Kirisako, T., Ichimura, Y., Okada, H., Kabeya, Y., Mizushima, N., Yoshimori, T., Ohsumi, M., Takao, T., Noda, T., and Ohsumi, Y. (2000). The reversible modification regulates the membrane-binding state of Apg8/Aut7 essential for autophagy and the cytoplasm to vacuole targeting pathway. J. Cell Biol. *151*, 263–276.

Klionsky, D.J., Abdelmohsen, K., Abe, A., Abedin, M.J., Abeliovich, H., Acevedo Arozena, A., Adachi, H., Adams, C.M., Adams, P.D., Adeli, K., et al. (2016). Guidelines for the use and interpretation of assays for monitoring autophagy (3rd edition). Autophagy *12*, 1–222.

Koushika, S.P., Schaefer, A.M., Vincent, R., Willis, J.H., Bowerman, B., and Nonet, M.L. (2004). Mutations in Caenorhabditis elegans cytoplasmic dynein components reveal specificity of neuronal retrograde cargo. J. Neurosci. *24*, 3907–3916.

Kumanomidou, T., Mizushima, T., Komatsu, M., Suzuki, A., Tanida, I., Sou, Y.S., Ueno, T., Kominami, E., Tanaka, K., and Yamane, T. (2006). The crystal structure of human Atg4b, a processing and de-conjugating enzyme for autophagosome-forming modifiers. J. Mol. Biol. *355*, 612–618.

Landis, S.C., Amara, S.G., Asadullah, K., Austin, C.P., Blumenstein, R., Bradley, E.W., Crystal, R.G., Darnell, R.B., Ferrante, R.J., Fillit, H., et al. (2012). A call for transparent reporting to optimize the predictive value of preclinical research. Nature *490*, 187–191.

Laurent, P., Soltesz, Z., Nelson, G.M., Chen, C., Arellano-Carbajal, F., Levy, E., and de Bono, M. (2015). Decoding a neural circuit controlling global animal state in C. elegans. Elife *4*.

Lee, S., Sato, Y., and Nixon, R.A. (2011). Lysosomal proteolysis inhibition selectively disrupts axonal transport of degradative organelles and causes an Alzheimer's-like axonal dystrophy. J. Neurosci. *31*, 7817–7830.

Li, M., Hou, Y., Wang, J., Chen, X., Shao, Z.M., and Yin, X.M. (2011). Kinetics comparisons of mammalian Atg4 homologues indicate selective preferences toward diverse Atg8 substrates. J. Biol. Chem. *286*, 7327–7338.

Liu, B., Du, H., Rutkowski, R., Gartner, A., and Wang, X. (2012). LAAT-1 is the lysosomal lysine/arginine transporter that maintains amino acid homeostasis. Science *337*, 351–354.

Luo, L., Cook, N., Venkatachalam, V., Martinez-Velazquez, L.A., Zhang, X., Calvo, A.C., Hawk, J., MacInnis, B.L., Frank, M., Ng, J.H., et al. (2014). Bidirectional thermotaxis in Caenorhabditis elegans is mediated by distinct sensorimotor strategies driven by the AFD thermosensory neurons. Proc. Natl. Acad. Sci. USA *111*, 2776–2781.

Maday, S., and Holzbaur, E.L. (2014). Autophagosome biogenesis in primary neurons follows an ordered and spatially regulated pathway. Dev. Cell *30*, 71–85.

Maday, S., Wallace, K.E., and Holzbaur, E.L. (2012). Autophagosomes initiate distally and mature during transport toward the cell soma in primary neurons. J. Cell Biol. *196*, 407–417.

Maniar, T.A., Kaplan, M., Wang, G.J., Shen, K., Wei, L., Shaw, J.E., Koushika, S.P., and Bargmann, C.I. (2011). UNC-33 (CRMP) and ankyrin organize microtubules and localize kinesin to polarize axon-dendrite sorting. Nat. Neurosci. *15*, 48–56.

Manil-Ségalen, M., Lefebvre, C., Jenzer, C., Trichet, M., Boulogne, C., Satiat-Jeunemaitre, B., and Legouis, R. (2014). The C. elegans LC3 acts downstream of GABARAP to degrade autophagosomes by interacting with the HOPS subunit VPS39. Dev. Cell *28*, 43–55.

Mariño, G., Uría, J.A., Puente, X.S., Quesada, V., Bordallo, J., and López-Otín, C. (2003). Human autophagins, a family of cysteine proteinases potentially implicated in cell degradation by autophagy. J. Biol. Chem. *278*, 3671–3678.

Maruyama, T., and Noda, N.N. (2017). Autophagy-regulating protease Atg4: structure, function, regulation and inhibition. J. Antibiot. *71*, 72–78.

Meléndez, A., Tallóczy, Z., Seaman, M., Eskelinen, E.L., Hall, D.H., and Levine, B. (2003). Autophagy genes are essential for Dauer development and life-span extension in C. elegans. Science *301*, 1387–1391.

Minevich, G., Park, D.S., Blankenberg, D., Poole, R.J., and Hobert, O. (2012). CloudMap: a cloud-based pipeline for analysis of mutant genome sequences. Genetics *192*, 1249–1269.

Miranda, A.M., Lasiecka, Z.M., Xu, Y., Neufeld, J., Shahriar, S., Simoes, S., Chan, R.B., Oliveira, T.G., Small, S.A., and Di Paolo, G. (2018). Neuronal lysosomal dysfunction releases exosomes harboring APP C-terminal fragments and unique lipid signatures. Nat. Commun. *9*, 291.

Mizushima, N., Yoshimori, T., and Levine, B. (2010). Methods in mammalian autophagy research. Cell *140*, 313–326.

Nakamura, S., and Yoshimori, T. (2017). New insights into autophagosome-lysosome fusion. J. Cell Sci. *130*, 1209–1216.

Nath, S., Dancourt, J., Shteyn, V., Puente, G., Fong, W.M., Nag, S., Bewersdorf, J., Yamamoto, A., Antonny, B., and Melia, T.J. (2014). Lipidation of the LC3/GABARAP family of autophagy proteins relies on a membrane-curvature-sensing domain in Atg3. Nat. Cell Biol. *16*, 415–424.

Neisch, A.L., Neufeld, T.P., and Hays, T.S. (2017). A STRIPAK complex mediates axonal transport of autophagosomes and dense core vesicles through PP2A regulation. J. Cell Biol. *216*, 441–461.

Nikoletopoulou, V., Sidiropoulou, K., Kallergi, E., Dalezios, Y., and Tavernarakis, N. (2017). Modulation of autophagy by BDNF underlies synaptic plasticity. Cell Metab. *26*, 230–242.

Nixon, R.A., Wegiel, J., Kumar, A., Yu, W.H., Peterhoff, C., Cataldo, A., and Cuervo, A.M. (2005). Extensive involvement of autophagy in Alzheimer disease: an immuno-electron microscopy study. J. Neuropathol. Exp. Neurol. *64*, 113–122.

Ojha, C.R., Lapierre, J., Rodriguez, M., Dever, S.M., Zadeh, M.A., DeMarino, C., Pleet, M.L., Kashanchi, F., and El-Hage, N. (2017). Interplay between autophagy, exosomes and HIV-1 associated neurological disorders: new insights for diagnosis and therapeutic applications. Viruses *9*, https://doi.org/10.3390/v9070176.

Okerlund, N.D., Schneider, K., Leal-Ortiz, S., Montenegro-Venegas, C., Kim, S.A., Garner, L.C., Waites, C.L., Gundelfinger, E.D., Reimer, R.J., and Garner, C.C. (2017). Bassoon controls presynaptic autophagy through Atg5. Neuron *93*, 897–913.

Pokala, N., Liu, Q., Gordus, A., and Bargmann, C.I. (2014). Inducible and titratable silencing of Caenorhabditis elegans neurons in vivo with histamine-gated chloride channels. Proc. Natl. Acad. Sci. USA *111*, 2770–2775.

Ponpuak, M., Mandell, M.A., Kimura, T., Chauhan, S., Cleyrat, C., and Deretic, V. (2015). Secretory autophagy. Curr. Opin. Cell Biol. *35*, 106–116.

Poteryaev, D., Fares, H., Bowerman, B., and Spang, A. (2007). Caenorhabditis elegans SAND-1 is essential for RAB-7 function in endosomal traffic. EMBO J *26*, 301–312.

Qi, Y.B., Garren, E.J., Shu, X., Tsien, R.Y., and Jin, Y. (2012). Photo-inducible cell ablation in Caenorhabditis elegans using the genetically encoded singlet oxygen generating protein miniSOG. Proc. Natl. Acad. Sci. USA *109*, 7499–7504.

Rolls, M.M., Hall, D.H., Victor, M., Stelzer, E.H., and Rapoport, T.A. (2002). Targeting of rough endoplasmic reticulum membrane proteins and ribosomes in invertebrate neurons. Mol. Biol. Cell *13*, 1778–1791.

Rowland, A.M., Richmond, J.E., Olsen, J.G., Hall, D.H., and Bamber, B.A. (2006). Presynaptic terminals independently regulate synaptic clustering and autophagy of GABAA receptors in Caenorhabditis elegans. J. Neurosci. *26*, 1711–1720.

Sarin, S., Prabhu, S., O'Meara, M.M., Pe'er, I., and Hobert, O. (2008). Caenorhabditis elegans mutant allele identification by whole-genome sequencing. Nat. Methods *5*, 865–867.

Satoh, Y., Sato, H., Kunitomo, H., Fei, X., Hashimoto, K., and Iino, Y. (2014). Regulation of experience-dependent bidirectional chemotaxis by a neural circuit switch in Caenorhabditis elegans. J. Neurosci. *34*, 15631–15637.

Schindelin, J., Arganda-Carreras, I., Frise, E., Kaynig, V., Longair, M., Pietzsch, T., Preibisch, S., Rueden, C., Saalfeld, S., Schmid, B., et al. (2012). Fiji: an open-source platform for biological-image analysis. Nat. Methods *9*, 676–682.

Shaner, N.C., Campbell, R.E., Steinbach, P.A., Giepmans, B.N.G., Palmer, A.E., and Tsien, R.Y. (2004). Improved monomeric red, orange and yellow fluorescent proteins derived from Discosoma sp. red fluorescent protein. Nat. Biotechnol. *22*, 1567–1572.

Shehata, M., Matsumura, H., Okubo-Suzuki, R., Ohkawa, N., and Inokuchi, K. (2012). Neuronal stimulation induces autophagy in hippocampal neurons that is involved in AMPA receptor degradation after chemical long-term depression. J. Neurosci. *32*, 10413–10422.

Shen, K., and Bargmann, C.I. (2003). The immunoglobulin superfamily protein SYG-1 determines the location of specific synapses in C. elegans. Cell *112*, 619–630.

Soukup, S.F., Kuenen, S., Vanhauwaert, R., Manetsberger, J., Hernández-Díaz, S., Swerts, J., Schoovaerts, N., Vilain, S., Gounko, N.V., Vints, K., et al. (2016). A LRRK2-dependent EndophilinA Phosphoswitch is critical for macroautophagy at presynaptic terminals. Neuron *92*, 829–844.

Stavoe, A.K., Hill, S.E., Hall, D.H., and Colón-Ramos, D.A. (2016). KIF1A/UNC-104 transports ATG-9 to regulate neurodevelopment and autophagy at synapses. Dev. Cell *38*, 171–185.

Stavoe, A.K.H., and Colón-Ramos, D.A. (2012). Netrin instructs synaptic vesicle clustering through Rac GTPase, MIG-10, and the actin cytoskeleton. J. Cell Biol. *197*, 75–88.

Sun, T., Li, Y., Li, T., Ma, H., Guo, Y., Jiang, X., Hou, M., Huang, S., and Chen, Z. (2017). JIP1 and JIP3 cooperate to mediate TrkB anterograde axonal transport by activating kinesin-1. Cell. Mol. Life Sci. *74*, 4027–4044.

Takáts, S., Nagy, P., Varga, Á., Pircs, K., Kárpáti, M., Varga, K., Kovács, A.L., Hegedűs, K., and Juhász, G. (2013). Autophagosomal Syntaxin17-dependent lysosomal degradation maintains neuronal function in Drosophila. J. Cell Biol. *201*, 531–539.

Tammineni, P., Ye, X., Feng, T., Aikal, D., and Cai, Q. (2017). Impaired retrograde transport of axonal autophagosomes contributes to autophagic stress in Alzheimer's disease neurons. Elife *6*.

Vanhauwaert, R., Kuenen, S., Masius, R., Bademosi, A., Manetsberger, J., Schoovaerts, N., Bounti, L., Gontcharenko, S., Swerts, J., Vilain, S., et al. (2017). The SAC1 domain in synaptojanin is required for autophagosome maturation at presynaptic terminals. EMBO J. *36*, 1392–1411.

Velikkakath, A.K., Nishimura, T., Oita, E., Ishihara, N., and Mizushima, N. (2012). Mammalian Atg2 proteins are essential for autophagosome formation and important for regulation of size and distribution of lipid droplets. Mol. Biol. Cell *23*, 896–909.

Wang, T., Martin, S., Papadopulos, A., Harper, C.B., Mavlyutov, T.A., Niranjan, D., Glass, N.R., Cooper-White, J.J., Sibarita, J.B., Choquet, D., et al. (2015). Control of autophagosome axonal retrograde flux by presynaptic activity unveiled using botulinum neurotoxin type a. J. Neurosci. *35*, 6179–6194.

Wang, Z., Miao, G., Xue, X., Guo, X., Yuan, C., Wang, Z., Zhang, G., Chen, Y., Feng, D., Hu, J., et al. (2016). The Vici syndrome protein EPG5 is a Rab7 effector that determines the fusion specificity of autophagosomes with late endosomes/lysosomes. Mol. Cell *63*, 781–795.

Weimer, R.M. (2006). Preservation of C. elegans tissue via high-pressure freezing and freeze-substitution for ultrastructural analysis and immunocytochemistry. Methods Mol. Biol. *351*, 203–221.

White, J.G., Southgate, E., Thomson, J.N., and Brenner, S. (1986). The structure of the nervous system of the nematode Caenorhabditis elegans. Philos. Trans. R. Soc. Lond. B Biol. Sci. *314*, 1–340.

Wu, F., Li, Y., Wang, F., Noda, N.N., and Zhang, H. (2012). Differential function of the two Atg4 homologues in the aggrephagy pathway in Caenorhabditis elegans. J. Biol. Chem. *287*, 29457–29467.

Zhang, H., Chang, J.T., Guo, B., Hansen, M., Jia, K., Kovács, A.L., Kumsta, C., Lapierre, L.R., Legouis, R., Lin, L., et al. (2015). Guidelines for monitoring autophagy in Caenorhabditis elegans. Autophagy *11*, 9–27.

Zhang, L., Li, J., Ouyang, L., Liu, B., and Cheng, Y. (2016). Unraveling the roles of Atg4 proteases from autophagy modulation to targeted cancer therapy. Cancer Lett. *373*, 19–26.

STAR★METHODS

KEY RESOURCES TABLE

REAGENT or RESOURCE	SOURCE	IDENTIFIER
Chemicals, Peptides, and Recombinant Proteins		
Levamisol hydrochloride	Sigma-Aldrich	31742
Ethyl methanesulfonate (EMS)	Sigma-Aldrich	M0880
IPTG	AmericanBio	AB00841
Binding buffer (25mM Tris, pH7.6, 150mM NaCl, 10mM Imidazole, 1mM BME)	Modified from Wu et al., 2012	N/A
cOmplete™, EDTA-free Protease inhibitor cocktail tablet	Roche	11873580001
Nickel beads	Qiagen	1018244
Washing buffer (25mM Tris, pH 7.6, 150mM NaCl, 60mM Imidazole, 1mM BME)	Modified from Wu et al., 2012	N/A
Elution buffer (25mM Tris, pH 7.6, 150mM NaCl, 250mM Imidazole, 1mM BME)	Modified from Wu et al., 2012	N/A
Thrombin buffer (20 mM Tris, pH 7.6, 100 mM NaCl, 5 mM $MgCl_2$, 2 mM $CaCl_2$, 1 mM DTT)	Choy et al., 2012	N/A
Glutathione beads	Sigma Aldrich	G4501
Thrombin	Sigma Aldrich	T6884
SN buffer (20mM Tris, pH 7.6, 100mM NaCl, 5mM $MgCl_2$) containing 1 mM DTT	Choy et al., 2012	N/A
LDS Loading Buffer	ThermoFisher Scientific	NP007
1,2-dioleoyl-sn-glycero-3-phosphoethanolamine (DOPE)	Avanti Polar Lipids	850752
1-palmitoyl-2-oleoyl-glycero-3-phosphocholine (POPC)	Avanti Polar Lipids	857457
L-α-phosphatidylinositol (liver, bovine) (PI)	Avanti Polar Lipids	840042
Nycodenz	Accurate Chemical and Scientific Corp.	1002424
Experimental Models: Organisms/Strains		
C. elegans: *olaIs35* X [Pttx-3::egfp::lgg-1; Pttx-3::mCh])	Stavoe et al., 2016	DCR4750
C. elegans: *unc-13(e450)*; *olaIs35*	This paper	DCR5581
C. elegans: *olaEx3465* [Pmod-1::HisCl (30ng/ul)]; *olaIs35*	This paper	DCR5896
C. elegans: *dnc-1(or404)* IV	Caenorhabditis Genetics Center	EU1006
C. elegans: *dnc-1(or404)*; *olaIs35*	This paper	DCR5549
C. elegans: *unc-16(ju146)* III	Caenorhabditis Genetics Center	CZ3011
C. elegans: *unc-16(ju146)*; *olaIs35*	This paper	DCR5353
C. elegans: *unc-16(e109) III*	Caenorhabditis Genetics Center	CB109
C. elegans: *unc-16(e109)*; *olaIs35*	This paper	DCR5579
C. elegans: *unc-16(n730) III*	Caenorhabditis Genetics Center	MT1542
C. elegans: *unc-16(n730);olaIs35*	This paper	DCR5597
C. elegans: *jip-1(gk466982)* II	Caenorhabditis Genetics Center	VC40110
C. elegans: *jip-1(gk466982)*; *olaIs35*	This paper	DCR5650
C. elegans: *unc-116(e2310)* III	Caenorhabditis Genetics Center	FF41
C. elegans: *unc-116(e2310)*; *olaIs35*	This paper	DCR5440
C. elegans: *unc-14(e57)* I	Caenorhabditis Genetics Center	CB57
C. elegans: *unc-14(e57)*; *olaIs35*	This paper	DCR5454
C. elegans: *atg-4.1(bp501)* I	Caenorhabditis Genetics Center	HZ1685
C. elegans: *atg-4.1(bp501)*; *olaIs35*	This paper	DCR6360
C. elegans: *atg-4.1(gk127286)* I	Caenorhabditis Genetics Center	VC30126
C. elegans: *atg-4.1(gk127286)*; *olaIs35*	This paper	DCR5752

(*Continued on next page*)

Continued

REAGENT or RESOURCE	SOURCE	IDENTIFIER
C. elegans: *atg-4.1(gk127286)*; *unc-16(ju146)*; *olaIs35*	This paper	DCR6134
C. elegans: *atg-4.2(gk430078)* IV	Caenorhabditis Genetics Center	VC30172
C. elegans: *atg-4.2(gk430078)*; *olaIs35*	This paper	DCR5649
C. elegans: *atg-4.2(gk628327)* IV	Caenorhabditis Genetics Center	VC40419
C. elegans: *atg-4.2(gk628327)*; *olaIs35*	This paper	DCR6874
C. elegans: *unc-16(ju146)*; *atg-4.2(gk628327)*; *olaIs35*	This paper	DCR6876
C. elegans: *atg-4.2(ola316)* IV	This paper	DCR5765
C. elegans: *atg-4.2(ola316)*; *olaIs35*	This paper	DCR5551
C. elegans: unc-16(ju146); atg-4.2(ola316); olaIs35	This paper	DCR5652
C. elegans: *atg-4.2(ola316)/nT1[qIs51]; atg-4.1(bp501); olaIs35*	This paper	DCR6390
C. elegans: *atg-4.2(gk430078)/nT1[qIs51]; atg-4.1(bp501); olaIs35*	This paper	DCR6391
C. elegans: *sand-1(or552)*	Caenorhabditis Genetics Center	FA85
C. elegans: *sand-1(or552)*; *olaIs35*	This paper	DCR6672
C. elegans: *unc-16(ju146)*; *sand-1(or552)*; *olaIs35*	This paper	DCR6736
C. elegans: *epg-5(tm3425); olaIs35*	Stavoe et al., 2016	DCR4859
C. elegans: *atg-4.2(gk628327)*; *epg-5(tm3425)*; *olaIs35*	This paper	DCR7240
C. elegans: *atg-2(bp576)*; *olaIs35*	Stavoe et al., 2016	DCR4906
C. elegans: *unc-16(ju146)*; *atg-2(bp576)*; *olaIs35*	This paper	DCR5770
C. elegans: *atg-9(wy56);olaIs35*	Stavoe et al., 2016	DCR4851
C. elegans: *atg-4.2(gk628327)*; *atg-9(wy56)*; *olaIs35*	This paper	DCR7365
C. elegans: *olaEx3430* [Pttx-3::atg-4.2 (30ng/ul)]; *olaIs35*	This paper	DCR5843
C. elegans: *olaEx3438* [Pttx-3::atg-4.2 (30ng/ul)]; *atg-4.2 (ola316); olaIs35*	This paper	DCR5854
C. elegans: *olaEx3426* [Pttx-3::atg-4.2(G1117A) (30ng/ul)]; *olaIs35*	This paper	DCR5833
C. elegans: *olaEx3293* [Pelt-7::gfp (10ng/ul)]; *olaIs35*	This paper	DCR5559
C. elegans: *olaEx3986* [Pttx-3::mCh::rab-3 (30ng/ul)]; *olaIs44* [Pttx-3::egfp::lgg-1 (15ng/ul)]	This paper	DCR6670
C. elegans: *olaEx4440* [Pmod-1::gfp::lgg-1(G116A) (5ng/ul), Pttx-3::mCh (30ng/ul)]	This paper	DCR7354
C. elegans: olaEx4440; atg-4.2(ola316)	This paper	DCR7393
C. elegans: *olaEx4440*; *atg-4.2(gk628327)*	This paper	DCR7394
C. elegans: *olaEx4440*; *epg-5(tm3425)*	This paper	DCR7395
C. elegans: *olaEx4440*; *sand-1(or552)*	This paper	DCR7396
C. elegans: *olaEx4440*; *unc-16(ju146)*	This paper	DCR7397
C. elegans: *olaEx4440*; *unc-16(n730)*	This paper	DCR7398
C. elegans: *olaEx4440*; *atg-4.1(bp501)*	This paper	DCR7411
C. elegans: *olaEx4493* [Pttx-3::gfp::syd-1A (15 ng/ul), Pttx-3::mCh::lgg-1 (20ng/ul)]	This paper	DCR7457
C. elegans: *olaEx4493*; *atg-4.2(ola316)*	This paper	DCR7470
C. elegans: *olaEx4472* [Pttx-3::gfp::snb-1 (3 ng/ul), Pttx-3::mCh::lgg-1 (20ng/ul)]	This paper	DCR7415
C. elegans: *olaEx4472*; *atg-4.2(ola316)*	This paper	DCR7462
C. elegans: *olaEx3013* [Pttx-3::mCh::egfp::lgg-1) (1ng/ul)]	This paper	DCR5074
C. elegans: *olaEx3013*; *atg-4.2(ola316)*	This paper	DCR6384
C. elegans: *olaEx3013*; *atg-4.1(bp501)*	This paper	DCR7125
C. elegans: *olaEx3013*; *atg-4.2(gk628327)*	This paper	DCR7362
C. elegans: *olaEx3013*; *sand-1(or552)*	This paper	DCR7065
C. elegans: *olaEx3013*; *epg-5(tm3425)*	This paper	DCR7064
C. elegans: *olaEx3015* [Pttx-3::mCh::egfp::lgg-1(G116A)) (1ng/ul)]	This paper	DCR5077

(*Continued on next page*)

Continued

REAGENT or RESOURCE	SOURCE	IDENTIFIER
C. elegans: *olaEx4354* [Pttx-3::laat-1::gfp (1ng/ul), Pttx-3::mCh::lgg-1 (20ng/ul)]	This paper	DCR7225
C. elegans: *olaEx4354*; *atg-4.2(gk628327)*	This paper	DCR7419
C. elegans: *olaEx4354; atg-4.2(ola316)*	This paper	DCR7421
C. elegans: *olaEx4431* [Pttx-3::mCh::egfp::lgg-1 (1ng/ul), Pttx-3::laat-1::tagbfp (2ng/ul)]	This paper	DCR7345
C. elegans: *olaEx4431*; *atg-4.2(ola316)*	This paper	DCR7404
C. elegans: *olaEx4374* [Pttx-3::mCh::egfp::lgg-1(G116A) (1ng/ul), Pttx-3::laat-1::tagbfp (1ng/ul)]	This paper	DCR7252
C. elegans: *olaEx4496* [Pttx-3::mCh::egfp::syd-1A (10ng/ul)]	This paper	DCR7460
C. elegans: *olaEx4496*; *atg-4.2(ola316)*	This paper	DCR7468
C. elegans: *olaEx1802* [Pttx-3::gfp::lgg-2 (30ng/ul), Pttx-3::mCh (30ng/ul)]	This paper	DCR3114
C. elegans: *olaEx1802*; *unc-16(ju146)*	This paper	DCR7215
C. elegans: *olaEx1802*; *unc-16(n730)*	This paper	DCR7265
C. elegans: *olaEx1802*; *atg-4.1(bp501)*	This paper	DCR7213
C. elegans: *olaEx1802*; *atg-4.2(ola316)*	This paper	DCR7214
C. elegans: *olaEx1802*; *atg-4.2(gk628327)*	This paper	DCR7256
C. elegans: *olaEx4438* [Pttx-3::gfp::lgg-2(G130A) (15ng/ul), Pttx-3::mCh (30ng/ul)]	This paper	DCR7352
C. elegans: *olaEx4456* [Pttx-3::gfp::syd-2 (15 ng/ul), Pttx-3::mCh::lgg-1 (20ng/ul)]	This paper	DCR7378
C. elegans: *olaEx4456*; *atg-4.2(ola316)*	This paper	DCR7455
C. elegans: *olaEx3358* [Pttx-3::ebp-2::gfp (5ng/ul), pttx-3::mCh (30ng/ul)]	This paper	DCR5675
C. elegans: *olaEx3358*; *unc-16(ju146)*	This paper	DCR5757
C. elegans: *olaEx3331* [Pttx-3::laat-1::gfp (1ng/ul), Pttx-3::mCh (30ng/ul)]	This paper	DCR5616
C. elegans: *olaEx3331*; *unc-16(ju146)*	This paper	DCR5651
C. elegans: *olaEx1706* [Pttx-3::SP12::gfp (5ng/ul)]	This paper	DCR2843
C. elegans: *olaex1706*; *unc-16(ju146)*	This paper	DCR5972
C. elegans: *olaEx1700* [Pttx-3:aman-2:gfp (0.5 ng/ul)]	This paper	DCR2837
C. elegans: *olaex1700*; *unc-16(ju146)*	This paper	DCR5968
C. elegans: *olaEx1951* [Pttx-3::tom-20::gfp (30 ng/ul), Pttx-3:mCh:rab-3 (30 ng/uL)]	This paper	DCR3373
C. elegans: *olaex1951*; *unc-16(ju146)*	This paper	DCR5974
C. elegans: *olaIs58* [Paex-3::egfp::lgg-1 (15ng/ul)]	This paper	DCR5495
C. elegans: *olaIs58*; *unc-16(ju146)*	This paper	DCR5582
C. elegans: *olaIs58*; *atg-4.2(ola316)*	This paper	DCR5892
C. elegans: *olaIs58*; *atg-4.2(ola316)*; *unc-16(ju146)*	This paper	DCR6169
C. elegans: *olaEx3644* [Pttx-3::atg-4.1B::gfp (20ng/ul)]	This paper	DCR6199
C. elegans: *olaEx3648* [Pttx-3::atg-4.2::gfp (20ng/ul)]	This paper	DCR6203
C. elegans: *wyIs45* [Pttx-3:gfp:rab-3]	Colon-Ramos et al., 2007	TV392
C. elegans: *wyIs45*; *atg-4.2(gk430078)*	Stavoe et al., 2016	DCR2323
C. elegans: *wyIs45*; *atg-4.2(ola316)*	This paper	DCR5858
C. elegans: *wyIs45*; *atg-4.1(gk127286)*	Stavoe et al., 2016	DCR2322
C. elegans: *wyIs45*; *atg-9(wy56)*	Stavoe et al., 2016	DCR1468
C. elegans: *wyIs45*; *atg-4.1(gk127286)*; *atg-4.2(gk430078)*	Stavoe et al., 2016	DCR2832
C. elegans: *wyIs45*; *atg-4.1(bp501)*	This paper	DCR6347
C. elegans: *wyIs45*; *sand-1(or552)*	This paper	DCR1510

(*Continued on next page*)

Continued

REAGENT or RESOURCE	SOURCE	IDENTIFIER
Oligonucleotides		
Genotyping primers	This paper, See Table S1	N/A
Recombinant DNA		
Plasmid: Pttx-3:eGFP:lgg-1	Stavoe et al., 2016	DACR1321
Plasmid: Pmod-1::HisCl	This paper	DACR1963
Plasmid: Pttx-3::atg-4.2	This paper	DACR1426
Plasmid: Pttx-3::atg-4.2(G1117A)	This paper	DACR2458
Plasmid: Pmod-1::gfp::lgg-1(G116A)	Stavoe et al., 2016	DACR2196
Plasmid: Pttx-3::GFP::syd-1A	This paper	DACR3153
Plasmid: Pttx-3::mCh::lgg-1	This paper	DACR2099
Plasmid: Pttx-3::gfp::snb-1	This paper	DACR2736
Plasmid: Pttx-3::mCh::egfp::lgg-1	This paper	DACR2199
Plasmid: Pttx-3::mCh::egfp::lgg-1(G116A)	This paper	DACR2204
Plasmid: Pttx-3::laat-1::gfp	This paper	DACR1669
Plasmid: Pttx-3::laat-1::tagbfp	This paper	DACR2899
Plasmid: Pttx-3::mCh::egfp::syd-1A	This paper	DACR3154
Plasmid: Pttx-3::gfp::lgg-2	This paper	DACR1288
Plasmid: Pttx-3::gfp::lgg-2(G130A)	This paper	DACR3113
Plasmid: Pttx-3::ebp-2::gfp	This paper	DACR2441
Plasmid: Paex-3::egfp::lgg-1	This paper	DACR2239
Plasmid: Pttx-3::atg-4.1B::gfp	This paper	DACR2564
Plasmid: Pttx-3::atg-4.2::gfp	This paper	DACR1492
Software and Algorithms		
Volocity	Improvision by Perkin Elmer	N/A
Adobe Photoshop	Adobe	CS4 and CS6
(Fiji is Just) ImageJ (FIJI)	Schindelin et al., 2012	https://fiji.sc/
PyMOL Molecular Graphics System Version 2.1.1	Schrodinger LLC	https://pymol.org
PRISM 7	Graphpad Software Inc	https://www.graphpad.com/
Other		
UltraView VoX spinning disc confocal microscope with a 60x CFI Plan Apo VC, NA 1.4, oil objective on a NikonTi-E stand	PerkinElmer	N/A
Hammamatsu C9100-50 camera	Hammamatsu	N/A
Electron microscope: JEOL JEM-1220 TEM	JEOL USA, MA	N/A
Ultramicrotome: Leica EM UC6	Leica Microsystems, IL	N/A
Knife: Diatome Ultra 45 Diamond Knife	Diatome, PA	N/A
Grids: FCF2010-CU-50 FORMVAR/CARBON 2X1MM CU 50/BX	Electron Microscopy Sciences, PA	N/A
Substitution: Leica AFS2	Leica Microsystems, IL	N/A

CONTACT FOR REAGENT AND RESOURCE SHARING

Further information and requests for resources and reagents should be directed to and will be fulfilled by the Lead Contact, Daniel A. Colón-Ramos (daniel.colon-ramos@yale.edu).

EXPERIMENTAL MODEL AND SUBJECT DETAILS

C. elegans Strains and Genetics

All *C. elegans* strains were raised on NGM plates with OP50 *Escherichia coli* as a food source, kept at 20°C, unless otherwise noted, and analyzed as larval 4 (L4) stage animals. We used N2 Bristol as the wild-type reference strain. We used the balancer nT1[qIs51]

isolated from VC3476 to assess escapers from *olaIs35; atg-4.1; atg-4.2/nT1*, which is sterile in its unbalanced state. For a full list of strains used in this study, please see the Key Resources Table.

Molecular Biology and Transgenic Lines

The plasmids used in this study for the creation of transgenic lines are derived from the pSM vector (Shen and Bargmann, 2003). We created transgenic strains using standard injection techniques. We used the following plasmids as co-injection markers: *Punc-122::gfp* (10-15ng/ul) and *Punc-122::dsRed* (30ng/ul). We also generated *olaEx3293* [Pelt-7::gfp (10ng/ul)] to distinguish heterozygous cross offspring from self progeny for the dominant/recessive tests.

For a full list of transgenic strains used in this study, please see the Key Resources Table.

For the cDNA constructs generated for use in this study (ATG-4.2, ATG-4.1B, LAAT-1 and EBP-2), we PCR amplified cDNA from a mixed stage population of *C. elegans*. A Q5 mutagenesis kit (NEB) was then used to introduce the DNA mutation G1117A (which corresponds to the allelic lesion in *atg-4.2(ola316)*) into the ATG-4.2 cDNA. The introduction of this lesion should result in expression of the mutant protein ATG-4.2(G373R). See the Key Resources Table for a plasmid list. Detailed sub-cloning information is available upon request.

METHOD DETAILS

Fluorescence Microscopy and Confocal Imaging

We used an UltraView VoX spinning disc confocal microscope with a 60x CFI Plan Apo VC, NA 1.4, oil objective on a NikonTi-E stand (PerkinElmer) with a Hammamatsu C9100-50 camera. We imaged the following fluorescently tagged fusion proteins, eGFP, GFP, RFP, tagBFP and mCherry at 405, 488 or 561 nm excitation wavelength. For three-channel imaging, in addition to eGFP and mCh, we expressed a worm-optimized blue fluorophore, tagBFP (Chai et al., 2012), kindly provided by the Shen lab at Stanford University). For experiments involving colocalization on punctate structures, we acquired channels first then z slices. We anesthetized *C. elegans* at room temperature in 10mM levamisole (Sigma) or as indicated.

Images were obtained using Volocity software (Improvision by Perkin Elmer) and processed using Adobe Photoshop CS4 and (Fiji is Just) ImageJ (FIJI) software. Image processing included maximal projection, rotation, cropping, brightness/contrast, pseudo coloring, and making surface plots. Kymographs were made using the "reslice" function in FIJI. Between genotypes for compared groups the confocal laser and camera settings and the FIJI brightness/contrast settings were kept identical. All quantifications from confocal images were conducted on maximal projections of the raw data. All images are oriented anterior to the left and dorsal up.

The crystal structure of human ATG4B-LC3(1-120) (Kumanomidou et al., 2006) was visualized using PyMOL Molecular Graphics System Version 2.1.1 (Schrodinger LLC), using PDB: 2Z0D.

SNP Mapping and Whole-Genome Sequencing

We obtained mutant allele *atg-4.2(ola316)* from a visual forward genetic enhancer screen in the *unc-16(ju146); olaIs35* mutant background (integrated line *olaIs35* contains Pttx-3::egfp::lgg-1; Pttx-3::mCh). Ethyl methanesulfonate (EMS) mutagenesis was performed and animals were screened for enhanced number of autophagosomes (visualized with GFP::LGG-1) in the AIY neurite. F2 progeny were viewed on a Leica DM 5000 B compound microscope with an HCX PL APO 63x/1.40-0.60 oil objective.

The novel lesion *ola316* was out-crossed from the *unc-16* lesion and found to have an independent dominant cell body accumulation of autophagic vacuoles. We then used single-nucleotide polymorphism (SNP) mapping as described (Davis and Hammarlund, 2006; Davis et al., 2005) to map the *ola316* lesion. Briefly, this involves crossing mutant animals to a divergent strain, Hawaiian CB4865, and detecting sites of recombination via comparison of dissimilar SNPs. To avoid selecting heterozygous recombinants of the dominant lesion, we mapped loss of the *ola316* locus by selecting animals with the wild-type phenotype. SNP mapping was then repeated for verification by selecting and confirming homozygous animals with the *unc-16; ola316* enhanced phenotype.

We then performed whole-genome sequencing on *unc-16; ola316; olaIs35* animals and for comparison *unc-16; olaIs35* animals at the Yale Center for Genome Analysis (YCGA), as previous (Sarin et al., 2008). We analyzed the results with www.usegalaxy.org, the "Cloudmap Unmapped Mutant workflow (w/ subtraction of other strains)," (Minevich et al., 2012) and verified lesions by Sanger sequencing.

Electron Microscopy

Strains were prepared using high-pressure freeze (HPF) fixation as previously described (Weimer, 2006). Briefly, twenty to thirty young adult hermaphrodites were placed in specimen chambers filled with *Escherichia coli* and frozen at −180°C under high pressure (Leica SPF HPM 100). Samples then underwent freeze substitution (Reichert AFS, Leica, Oberkochen, Germany) using the following program: Samples were held at −90°C for 107 hours with 0.1% tannic acid and 2% OsO_4 in anhydrous acetone, then incrementally warmed at a rate of 5°C/hour to −20°C, and kept at −20°C for 14 hours, before increasing temperature by 10°C/hour to 20°C. After fixation, samples were infiltrated with 50% Epon/acetone for 4 hours, 90% Epon/acetone for 18 hours, and 100% Epon for 5 hours. Finally, samples were embedded in Epon and incubated for 48 hours at 65°C. Specimens were blinded for genotype prior to sectioning. Thin (70 nm) serial sections were cut using an Ultracut 6 (Leica) and collected on formvar-covered, carbon-coated copper grids (EMS, FCF2010-Cu). Post-staining was performed using 2.5% aqueous uranyl acetate for 4 minutes, followed by Reynolds lead

citrate for 2 minutes. Images were obtained on a Jeol JEM-1220 (Tokyo, Japan) transmission electron microscope operating at 80 kV. Micrographs were collected using a Gatan digital camera (Pleasanton, CA) at a magnification of 40 k.

Images were taken from 2 animals for each strain (*olaIs35* (wild-type control), *atg-4.2(ola316); olaIs35*, and *atg-4.1(bp501); olaIs35*), using the isthmus of the pharynx as a marker to locate neuronal cell bodies within the nerve ring (White et al., 1986). Image collection and scoring of multi-lamellar (autophagosome) structures was performed blinded to the genotype.

Purification of *C. elegans* Proteins

Mouse Atg3 and Atg7 proteins were purified as previously described (Horenkamp et al., 2015; Nath et al., 2014). In brief, mouse ATG3 was expressed with a GST tag in *E. coli*, and then affinity purified on a glutathione-bead column, eluted by cleavage of the GST, and mixed with 10% glycerol for storage at -80°C. Mouse ATG7 was expressed with a his-tag in a baculoviral system and then affinity purified on nickel resin, eluted by thrombin protease cleavage of the his-tag and mixed with 10% glycerol for storage at -80°C. The *C. elegans* His-ATG-4.2 was cloned into the pET28A vector for bacterial expression. *C. elegans* LGG-1(G116) and LGG-1-His were cloned into the pGEX-2T vector to include a thrombin-cleavable N-terminal GST to be used for affinity purification.

His-ATG-4.2 was then expressed as previously described for mammalian ATG4 proteins (Kauffman et al., 2018). Plasmids were transformed into BL21-Gold(DE3) *E. coli* (Agilent Technologies, 230132). Cells were grown to an OD of 0.6-0.8 at 37°C before induction with 0.2 mM IPTG (AmericanBio, AB00841) at 18°C overnight. Cells were then collected by centrifugation and resuspended in binding buffer (25mM Tris, pH7.6, 150mM NaCl, 10mM Imidazole, 1mM BME) also supplemented with a cOmplete™, EDTA-free Protease inhibitor cocktail tablet. Cells were lysed with a cell disruptor and cleared by centrifugation. Supernatants were incubated with nickel beads for 4h at 4°C. Beads were collected and washed three times with washing buffer (25mM Tris, pH 7.6, 150mM NaCl, 60mM Imidazole, 1mM BME) before elution with elution buffer (25mM Tris, pH 7.6, 150mM NaCl, 250mM Imidazole, 1mM BME). His-ATG4.2 was then stored at -80°C in 20% glycerol.

LGG-1(G116) and LGG-1-His were expressed as previously described for mammalian Atg8 homologues (Kauffman et al., 2018). Briefly, cells were resuspended in thrombin buffer (20 mM Tris, pH 7.6, 100 mM NaCl, 5 mM $MgCl_2$, 2 mM $CaCl_2$, 1 mM DTT), which was supplemented with a cOmplete™, EDTA-free Protease inhibitor cocktail tablet (Roche, 11873580001). Cells were lysed using a cell disruptor and cleared by centrifugation. The supernatant was incubated with glutathione beads (Sigma Aldrich, G4501) for 4 hours at 4°C. Beads were collected and washed three times with thrombin buffer before the addition of thrombin (Sigma Aldrich, T6884). Thrombin was allowed to cut at 4°C overnight. Fractions of LGG-1(G116) or LGG-1-His were then collected and stored at -80°C in 20% glycerol.

Proteoliposome Preparation

Liposomes were prepared as previously described and all lipids were purchased from Avanti (Kauffman et al., 2018). Briefly, lipids were mixed to obtain a composition of 55 mol percent 1,2-dioleoyl-sn-glycero-3-phosphoethanolamine (DOPE), 35 mol percent 1-palmitoyl-2-oleoyl-glycero-3-phosphocholine (POPC), and 10 mol percent L-α-phosphatidylinositol (liver, bovine) (PI) and dried to a thin film under nitrogen. The lipid film was dried for an hour under vacuum before resuspension in SN buffer (20mM Tris, pH 7.6, 100mM NaCl, 5mM $MgCl_2$) and subjected to seven freeze-thaw cycles. Liposomes were extruded to 400nm and further sonicated to $\leq$ 50nm immediately prior to the lipidation reaction. LGG-1(G116) (15μM), mAtg3 (2μM), mAtg7 (2 μM), and sonicated liposomes (3 mM) were mixed in SN buffer containing 1 mM DTT. Lipidation was initiated by adding 1 mM ATP and reactions were incubated at room temperature for 2 hours. Protein-conjugated liposomes were then purified using a Nycodenz Density gradient (Kauffman et al., 2018). The bottom layer of the gradient was composed of the lipidation reaction in 40% Nycodenz, the middle layer was 30% Nycodenz, and the top layer was SN buffer. Following ultracentrifugation, LGG-1-conjugated liposomes were collected from the 30% Nycodenz/buffer interface. LGG-1-conjugated liposomes were stored on ice at 4°C.

In Vitro Proteolysis Assays

LGG-1-conjugated liposomes or 7 μM LGG-1-His were incubated with 250nM His-Atg-4.2 in SN buffer at room temperature. Samples were removed at the indicated times and mixed with LDS Loading Buffer (ThermoFisher Scientific, NP007) and boiled to stop the reaction. Samples were then visualized using SDS-PAGE and Coomassie Brilliant Blue staining and were analyzed by densitometry using ImageJ. Graph displays the average of three independent assays with standard deviation.

QUANTIFICATION AND STATISTICAL ANALYSIS

Quantification of Autophagosomes in AIY

Quantifications were performed taking into consideration best practices as suggested in (Landis et al., 2012), including randomization, blinding, and data handling procedures. Particulars for each assay as follows:

Activity-dependent Autophagy

To assess synaptic autophagy, animals containing *olaIs35* in a wild-type, or *unc-13(e450)* mutant background were grown at 20°C and then shifted to 25°C for variable lengths of time (as indicated) and assessed for number of LGG-1 puncta in the AIY neurite on a Leica DM 5000 B compound microscope. For the HisCl experiments, the animals additionally contained the extrachromosomal array *olaEx3465* (Pmod-1::HisCl) and were transferred to 10mM histamine-containing or control NGM plates at 20°C or 25°C for 4 hours

prior to assessment (Pokala et al., 2014). Animals were then mounted in either 5 mM levamisole in M9 buffer (compared to 10 mM used in all other experiments) or in M9 buffer containing 5 mM levamisole and 10 mM histamine and scored blindly. Results are reported in Figures 1J and 1K.

AV Accumulation in Neurites and Cell Bodies

To investigate the accumulation of autophagosomes in the AIY neuron, we tested mutant alleles in the *olaIs35* (Pttx-3::egfp::lgg-1; Pttx-3::mCh) background. For the temperature sensitive *dnc-1(or404)* allele (Koushika et al., 2004) and a wild-type control, animals were held at either 20°C (permissive) or 25°C (restrictive) for 48 hours prior to examination and analyzed at larval stage 4 (L4). Other candidate transport mutant animals (*unc-16*, *jip-1*, *unc-116*, *unc-14* and controls) were kept at 20°C. Autophagosome accumulation in the neurite was then scored on a Leica DM 5000 B compound microscope. For each animal, the sum of autophagosomes in both AIY neurons was counted, then divided by two and reported as an average per neuron in Figures 2C and 2G. Additional quantifications (presented in Figures 3D–3E, 4E, 5G, 5H, S4I, S4R, S6J, and S6K) using the *olaIs35* background to detect presence of autophagosomes in the cell bodies and neurites of mutant animals (*unc-16*, *atg-4.2*, *atg-4.1*, *epg-5*, *sand-1* etc.), double mutant animals, and animals overexpressing ATG-4.2 arrays, were scored as follows: raw z-stacks were divided to separate individual AIY neurons, maximal projections were created, and images were randomized and scored blindly. The same method was used to assess the LGG-1(G116A) and LGG-2(G130A) lipidation controls, in *olaEx4440* [Pmod-1::gfp::lgg-1(G116A) (5ng/ul), Pttx-3::mCh (30ng/ul)] and *olaEx4438* [Pttx-3::gfp::lgg-2(G130A) (15ng/ul), Pttx-3::mCh (30ng/ul)], results described in the Figures S1 and S5 figure legends. For LGG-2-labeled autophagosomes in the *olaEx1802* [Pttx-3::gfp::lgg-2 (30ng/ul), Pttx-3::mCh (30ng/ul)] background (reported in Figures S2C–S2D and S4G–S4H), however, due to the variability in expression for the *olaEx1802* array in both wild-type and mutant animals, neurons were only assessed for puncta if the GFP::LGG-2 cytoplasmic signal was within the dynamic range for a chosen set of confocal laser and camera settings that were kept constant between all genotypes examined.

Autophagosome Dynamics

To assess autophagosome dynamics over time, we used the integrated line *olaIs35* (Pttx-3::egfp::lgg-1; Pttx-3::mCh). We imaged at maximal speed for 5 minutes in wild-type (n=71 neurons), *unc-16(*ju146*)* mutant (n=73 neurons), and *unc-16(*e109*)* mutant (n=43 neurons) animals. These videos were scored for percentage of autophagosomes present in each of the three sub-neurite zones (Figure 2I) (Colon-Ramos et al., 2007), for anterograde and retrograde directionality of autophagosome trafficking in the neurite (Figure 2L), and for percentage of autophagosomes leaving the cell body towards the neurite, and then returning to the cell body within the imaging window of 5 minutes (Figure S2H).

Tandem Markers and Colocalization Assays

For quantifications, images were acquired channels first then z slice (unless otherwise stated) and image settings were kept identical between compared groups. Raw z-stacks were then divided to separate individual AIY neurons and images were randomized and scored blindly. Puncta counts across neurons were then pooled and reported as percentages.

The tandem marker used in this study is based on similar probes used in mammalian neurons (Kimura et al., 2007) and in *C. elegans* tissues (Chang et al., 2017). Autophagosome maturation was assessed using extrachromosomal lines *olaEx3013* and *olaEx4431*. For *olaEx3013*, (Pttx-3::mCh::egfp::lgg-1) puncta were scored as "mCh/GFP" (immature) if green and red colocalized puncta could be detected and as "LGG-1 mCh" (mature) if the puncta displayed primarily red signal (reported in Figures 5W and S7H). For *olaEx4431* [Pttx-3::mCh::egfp::lgg-1 (1ng/ul), Pttx-3::laat-1::tagbfp (2ng/ul)], puncta were scored as "Immature AVL" if positive for tagBFP, mCherry and GFP, and as "Mature AL or L" if positive for tagBFP and mCherry, but negative for GFP (reported in Figure 6H).

To examine the tandem-labeled LGG-1 probe for lipidation onto membranes and to control for the possibility of marker aggregation, we also examined mutant versions of the tandem probe (*olaEx3015* (Pttx-3::mCh::egfp::lgg-1(G116A)) and *olaEx4374* [Pttx-3::mCh::egfp::lgg-1(G116A) (1ng/ul), Pttx-3::laat-1::tagbfp (1ng/ul)]), which prevents LGG-1 from associating with the autophagosomal membrane (Schematic in Figure S1D; Mizushima et al., 2010; Zhang et al., 2015). We observed that in the LGG-1(G116A) mutant probe, GFP was diffuse throughout the neuron (Figure S7A), indicating that lipidation is necessary for formation of LGG-1 puncta, and suggesting that most mCh::GFP::LGG-1 puncta correspond to autophagic vacuoles, as expected (Chang et al., 2017; Kimura et al., 2007).

We also note that for the tandem-labeled LGG-1 probe, we observed mCherry puncta in the cell body. We observed mCherry puncta even when the marker contained the LGG-1(G116A) point mutation that prevents LGG-1 lipidation and association with autophagosomes (Figure S7B). These mCherry puncta did not colocalize with GFP, indicating they do not simply correspond to protein aggregates of the tandem-labeled marker. Red fluorophores like mCherry are stable at low pH (Shaner et al., 2004) and accumulate in lysosomal compartments (Han et al., 2014; Katayama et al., 2008). Consistent with this, we observed that most mCh puncta from the LGG-1(G116A) tandem probe colocalized with lysosomes in the cell body (Figure S7A–S7D). Indeed, even cytoplasmic expression of mCherry resulted in accumulation of mCherry into puncta that colocalized with lysosomes (Figure S7E–S7G). Our findings indicate that mCherry accumulates in lysosomal compartments, and suggest that most of the observed non-lipidated mCh::GFP::LGG-1(G116A) puncta are inside acidic lysosomes.

To assess colocalization between LGG-1 and other proteins of interest, including lysosomal protein LAAT-1 (Liu et al., 2012) and synaptic proteins SYD-1, SYD-2, and SNB-1 (Dittman and Kaplan, 2006), we examined animals containing *olaEx4354* [Pttx-3::laat-1::gfp (1ng/ul), Pttx-3::mCh::lgg-1 (20ng/ul)] (data reported in Figures 6E and S7I), *olaEx4493* [Pttx-3::gfp::syd-1A (15 ng/ul),

Pttx-3::mCh::lgg-1 (20ng/ul)] (Figure 6I), *olaEx4472* [Pttx-3::gfp::snb-1 (3 ng/ul), Pttx-3::mCh::lgg-1 (20ng/ul)] (Figure S7R), and *olaEx4456* [Pttx-3::gfp::syd-2 (15 ng/ul), Pttx-3::mCh::lgg-1 (20ng/ul)] (Figure S7R). We also examined the acidification state of synaptic compartments by examining a tandem SYD-1 marker in *olaEx4496* [Pttx-3::mCh::egfp::syd-1A (10ng/ul)]. Puncta were scored as "SYD-1 mCh only" if positive for mCh and negative for GFP (acidic compartments) and "SYD-1 mCh/GFP" if positive for both GFP and mCh (non-acidified compartments) (reported in Figure 6M). To assess the percentage of mCh puncta inside lysosomes, we examined animals containing *olaEx3331* [Pttx-3::laat-1::gfp (1ng/ul), Pttx-3::mCh (30ng/ul)] (Figures S7E–S7G). Images were acquired z first, then channels, and puncta were only quantified if there was no detectable motion artifact, and if puncta were clearly distinguished from the cytosolic pool of mCherry signal. As a result, it is likely our results (81% of cytosolic mCh puncta colocalize with LAAT-1::GFP; n= 27 puncta from 9 neurons) under-sample mCherry puncta and might underestimate the extent to which mCh and LAAT-1 colocalize.

Other Quantifications in AIY

Microtubule EBP-2 Quantification

To examine microtubule polarity, we analyzed the direction of movement for EBP-2 comets (Baas and Lin, 2011; Maniar et al., 2011), which track with the growing ends of microtubules, along the AIY neurite using the extrachromosomal line *olaEx3358* (Pttx-3::ebp-2::gfp, Pttx-3::mCh). Confocal z-stacks were acquired at maximal speed for one minute and comets were assessed for movement towards the cell body (minus end out microtubule) or movement away from the cell body (plus end out microtubule) in wild-type (n=18 animals) and *unc-16* mutant animals (n=16 animals), and reported in Figure S2G.

Lysosomes

To quantify lysosome number in AIY, we observed the extrachromosomal transgenic line *olaEx3331* (Pttx-3::laat-1::gfp, pttx-3::mCh) in wild-type or mutant backgrounds on a Leica DM 5000 B compound microscope. The number of GFP puncta in the two AIY neurons in the animal were counted by location, divided by two and then reported as an average per neuron (Figure S3C).

Endoplasmic Reticulum, Golgi, Mitochondria

For examination of ER, Golgi, and mitochondria the following extrachromosomal lines were used, respectively: *olaEx1706* (Pttx-3::SP12::gfp), *olaEx1700* (Pttx-3:aman-2:gfp), and *olaEx1951* (Pttx-3::tom-20::gfp, pttx-3:mCh:rab-3) (Abe et al., 2000; Qi et al., 2012; Rolls et al., 2002) in wild-type and *unc-16(ju146)* mutant backgrounds. Quantifications were performed on maximal projections of confocal micrographs. Fluorescence intensity was measured by tracing the neurite and background in FIJI (Schindelin et al., 2012) and reported as an average of background-subtracted fluorescence intensity (Figure S3F and data not shown). The percent of the neurite occupied by mitochondria was calculated as a ratio of length of the neurite with background-subtracted fluorescence signal greater than zero divided by the total length of the neurite (Figure S3I).

Presynaptic Enrichment

To quantify presynaptic enrichment in AIY, we used the integrated transgenic line *wyIs45*, expressing pttx-3::gfp::rab-3 in wild-type and mutant backgrounds, as described (Colon-Ramos et al., 2007; Stavoe et al., 2016). The AIY neurite is divided into three zones as follows, consistent with the *C. elegans* EM reconstruction (White et al., 1986): Zone 1 is proximal to the cell body and asynaptic; Zone 2 is defined morphologically as a ~5-μm synapse-rich region at the dorsal turn of the neuron into the nerve ring; Zone 3 is the distal part of the neurite that traverses the nerve ring and contains punctate synaptic sites. We calculated the GFP::RAB-3 enrichment using maximal projection confocal micrographs and measured fluorescence intensity across presynaptic Zones 2 and 3 with the line scan function in FIJI (Schindelin et al., 2012). Fluorescence intensity was background subtracted. All settings, for the confocal microscope and camera, were kept identical between genotypes, and neurons were only quantified when all neurite fluorescence signal was within the measurable range. Synaptic enrichment was reported as signal in Zone 2 (the first 20% of the synaptic region) divided over Zones 2 and 3 (as described in Stavoe and Colon-Ramos, [2012]) and reported as a percentage and shown in Figure S6G.

Statistical Analyses

Statistical analyses were conducted with PRISM 7 software. For each case, the chosen statistical test is described in the figure legend and "n" values are reported. Briefly, for continuous data and for cases of counting structures, comparisons between two groups were determined by the Student's t test, while groups of three or more were analyzed with a one-way ANOVA with *post hoc* analysis by Turkey's multiple comparison test. Error bars were reported as standard errors of the mean (SEM). For categorical data, groups were compared with Fisher's exact test, or for samples corresponding to large datasets, the chi-square test was used. Error bars show a 95% confidence interval. Significance was defined as a p value where $p>0.05$. The p values for significant differences are reported in the figure legends.

Developmental Cell, Volume *49*

Supplemental Information

Maturation and Clearance of Autophagosomes in Neurons Depends on a Specific Cysteine Protease Isoform, ATG-4.2

Sarah E. Hill, Karlina J. Kauffman, Mia Krout, Janet E. Richmond, Thomas J. Melia, and Daniel A. Colón-Ramos

SUPPLEMENTAL FIGURES AND FIGURE LEGENDS

Figure S1

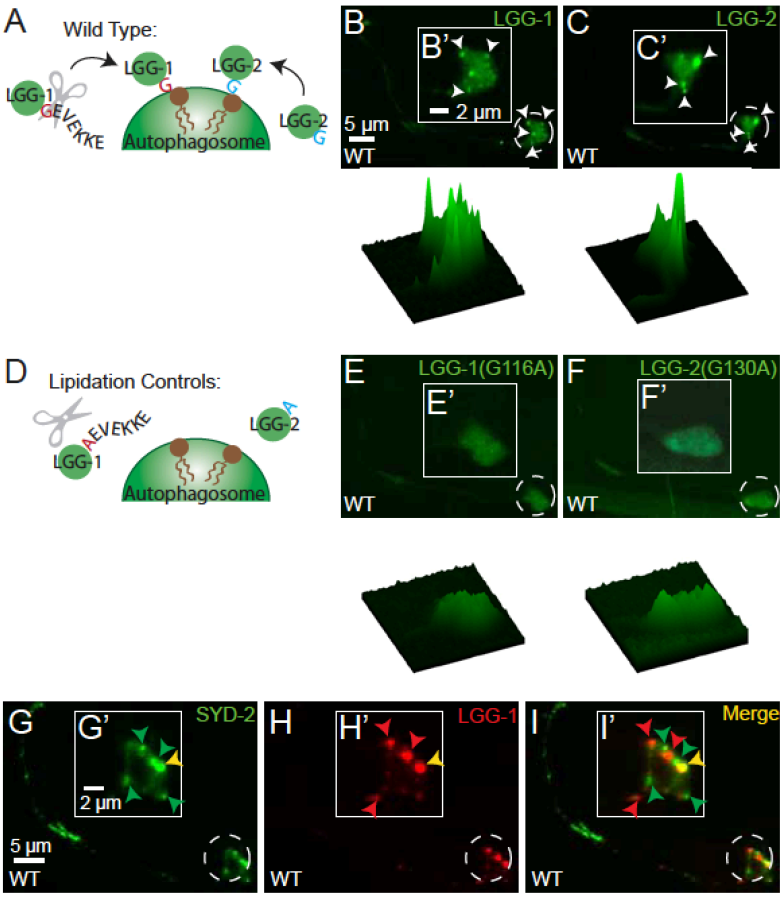

Figure S1. Autophagic structures in AIY neurons can be visualized with LGG-1 and LGG-2, related to Figure 1.

(A-F) Schematics of the lipidation processes for LGG-1 and LGG-2, showing the C-terminal priming of LGG-1 and lipidation at conserved glycines (A) and lipidation controls with mutations at G116A (LGG-1) or G130A (LGG-2), which fail to be primed or lipidated (D). In B, C, E, and F, representative autophagic vacuoles or lipidation controls are visualized with GFP::LGG-1 (B), GFP::LGG-2 (C), GFP::LGG-1(G116A) (E) or GFP::LGG-2(G130A) (F) in a representative wild-type AIY neuron. In B and C, arrowheads indicate LGG-1- and LGG-2-labeled autophagic structures in the cell body. Insets, B', C', E' and F' show the enlarged cell body (indicated in main image with dashed circle) with corresponding surface plots (below). Note that while we observed an average of 3.9 puncta in the cell bodies of neurons expressing GFP::LGG-1 (n=65 neurons; data from Figure 3E) and 4.6 puncta for GFP::LGG-2 (n=31 neurons; data from Figure S2D), in the corresponding lipidation controls GFP::LGG-1(G116A) and GFP::LGG-2(G130A), we observed an average of 0.07 puncta (n=14 neurons) or 0.05 puncta (n=21 neurons), respectively, suggesting that nearly all of the puncta we observed with LGG-1/LGG-2 were lipidated.

(G-I) Representative confocal image of presynaptic active zone protein GFP::SYD-2 (G) co-localized with mCh::LGG-1 (H). Merge images in (I). Insets in G'-I' show the enlarged cell body with subcellular localization of these proteins (indicated in main image with dashed circles).

Scale bar(s): in (B) for (B), (C), (E) and (F); in (B') for (B'), (C'), (E') and (F'); in (G) for (G)-(I); in (G') for (G')-(I').

Figure S2

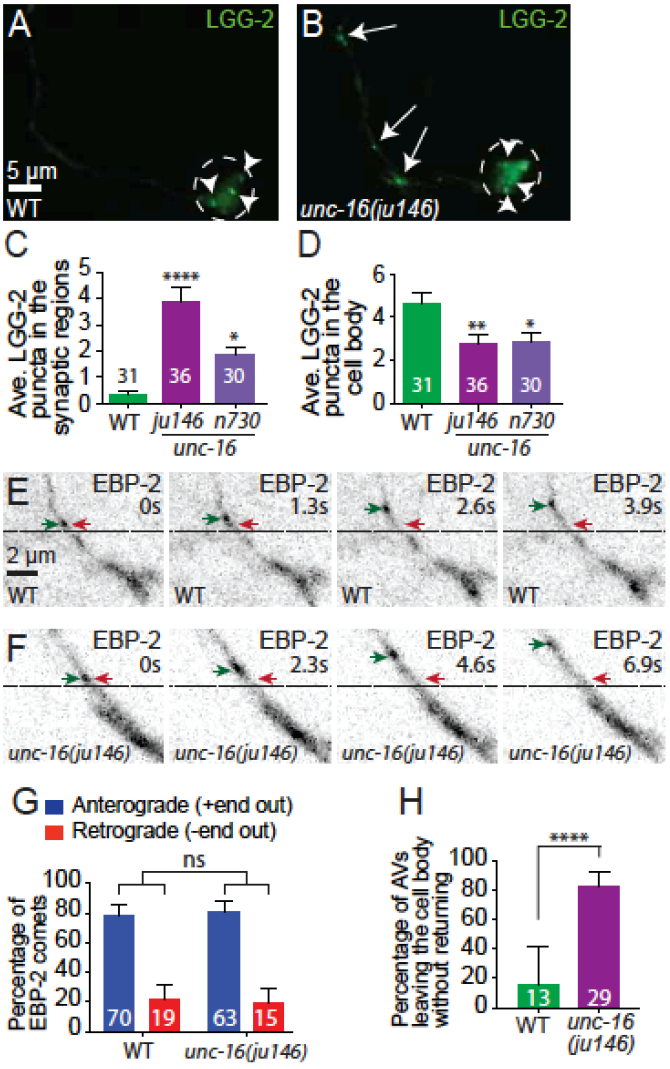

Figure S2. LGG-2 accumulates in the neurites of *unc-16/jip3* mutant animals, but microtubule polarity in AIY is unaltered, related to Figure 2.

(A and B) Autophagic vacuoles (visualized with GFP::LGG-2) in a representative wild-type AIY neuron (A) and in an *unc-16(ju146)* mutant neuron (B). Arrows denote LGG-2 puncta in the synaptic region; arrowheads denote LGG-2 puncta in the neuronal soma. Dashed circles enclose the cell bodies.

(C and D) Quantification of the average number of LGG-2 puncta in the synaptic regions (C) or cell bodies (D) in wild-type animals, and two alleles of *unc-16* (*ju146* and *n730*) mutant animals. Error bars show standard error of the mean (SEM). *p<0.05, **p<0.01, and p****p<0.0001 by one-way ANOVA with Tukey's post hoc analysis. The number of neurons examined is shown on each bar. Scoring was done by blindly quantifying maximal projections of confocal z-stacks. See also Figure S1.

(E and F) Time series of representative growing (+) ends of microtubules, visualized with (EBP-2::GFP) in wild-type (E) and *unc-16(ju146)* (F) mutant animals. We include dashed lines at the same position and across time points for reference. Red arrows denote EBP-2 puncta start positions. Green arrows track EBP-2 puncta positions over time. Time is indicated in the upper right corner of the image and "s" is seconds. Images are oriented distal axon towards the upper left, cell body towards the lower right.

(G) Quantification of the percentage of EBP-2 comets trafficking in the anterograde direction away from the cell body (corresponding microtubule is plus (+) end out) or the retrograde direction towards the cell body (corresponding microtubule is minus (-) end out) in wild-type and *unc-16(ju146)* mutant animals. The number of EBP-2 comets examined is shown on each bar for ≥16 animals for each genotype. Note that the AIY neurite shows a primarily plus-end-out microtubule orientation, which is a common feature of axons (Baas and Lin, 2011), and which is not altered in *unc-16(ju146)/jip3* mutant animals. "ns," not significant by Fisher's exact test between wild-type and mutant animals. Error bars show a 95% confidence interval.

(H) Quantification of the percentage of autophagosomes that traffic out of the cell body and do not return within the 5-minute imaging window in wild-type animals (n=13 autophagosomes) and *unc-16* mutant animals (n=29 autophagosomes). Error bars show a 95% confidence interval. ****$p<0.0001$ by Fisher's exact test between wild-type animals and mutant animals.

Scale bar(s): in (A) for (A) and (B); in (E) for (E) and (F).

Figure S3

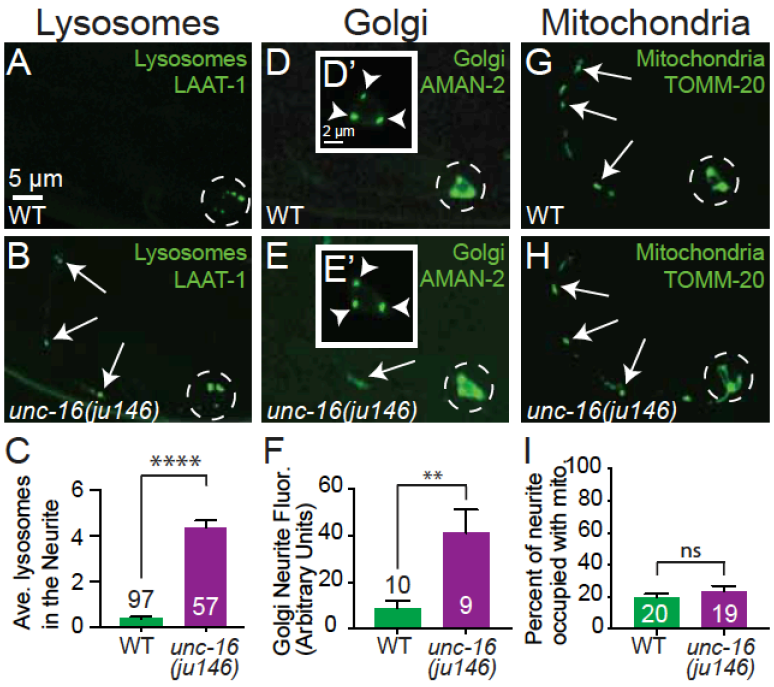

Figure S3. Organelle localizations in *unc-16/jip3* mutant animals, related to Figure 2.

(A and B) Representative images of lysosomes (visualized with LAAT-1::GFP) (Liu et al., 2012) in wild-type (A) and *unc-16(ju146)* mutant animals (B). Dashed circles enclose the cell bodies. Arrows denote lysosomes in the neurite.

(C) Quantification of the average number of lysosomes in the neurite of AIY in wild-type and *unc-16(ju146)* mutant animals. Error bars show standard error of the mean (SEM). ****p<0.0001 by Student's t test between wild-type and mutant animals. The number of animals examined is shown on each bar.

(D and E) Representative images of Golgi (visualized with AMAN-2::GFP) (Rolls et al., 2002) in wild-type (D) and *unc-16(ju146)* mutant animals (E). Dashed circles enclose the cell bodies. Arrow denotes AMAN-2::GFP in the neurite. Insets (D') in (D) and (E') in (E) show enlarged views of the cell body with different brightness and contrast as compared to the main image and adjusted to better visualize the cell body. Arrowheads denote Golgi puncta in the cell body. There was no significant difference in the number of cell body Golgi puncta between wild-type (2.5 puncta, n=10 neurons) and *unc-16(ju146)* (2.9 puncta, n=9 neurons) mutant animals.

(F) Quantification of background subtracted Golgi fluorescence signal in the neurite of AIY in wild-type and *unc-16(ju146)* mutant animals. Error bars show standard error of the mean (SEM). **p<0.01 by Student's t test between wild-type and mutant animals. The number of neurons examined is shown on each bar. We note that the neurite signal,

while brighter in *unc-16(ju146)* mutant animals, is faint and cytoplasmic rather than the expected punctate pattern seen in the cell body for Golgi stacks.

(G and H) Representative images of mitochondria (visualized with TOM20::GFP) (Abe et al., 2000; Qi et al., 2012) in wild-type (G) and *unc-16(ju146)* mutant animals (H). Dashed circles enclose the cell bodies. Arrows denote mitochondria in the neurite.

(I) Quantification of the percentage of the length of the AIY neurite occupied by mitochondria in wild-type and *unc-16(ju146)* mutant animals. Neurite fluorescence intensity analyses of the mitochondria revealed higher intensity for TOM20::GFP in *unc-16* mutant animals, similar to the results seen for the for the Golgi AMAN-2::GFP marker, but not an increase in mitochondria occupancy in the neurite. Analyses for the endoplasmic reticulum (ER) (visualized with SP12::GFP) (Rolls et al., 2002) revealed no significant difference in ER signal intensity in the neurites of wild-type and *unc-16(ju146)* mutant animals (data not shown). Error bars show standard error of the mean (SEM). “ns,” not significant by Student’s t test between wild-type and mutant animals. The number of neurons examined is shown on each bar.

Scale bar(s): in (A) for (A), (B), (D), (E), (G), and (H); in (D’) for (D’) and (E’).

Figure S4

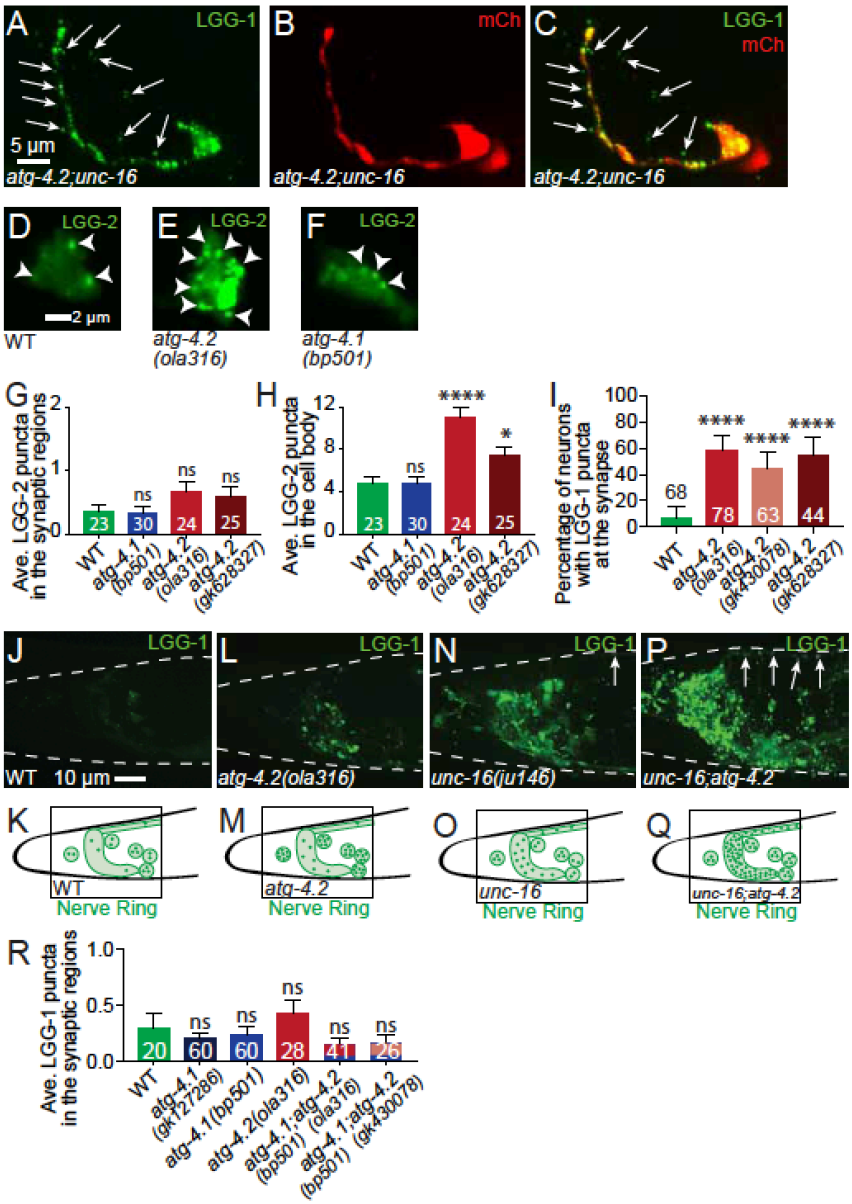

Figure S4. Autophagosome accumulation phenotypes in the neurites and cell bodies of *atg-4.2* mutant animals, related to Figure 3.

(A-C) Autophagic structures (visualized with GFP::LGG-1) (A) and AIY neuronal morphology (visualized with cytoplasmic mCherry) (B) in a representative *atg-4.2(ola316)*; *unc-16(ju146)* double mutant neuron. The merge image (C) reveals some GFP:LGG-1 signal located outside the AIY neuron (arrows), not normally seen in wild-type animals, and consistent with release or secretion of autophagic structures from AIY into the surrounding tissue (nerve ring environment or surrounding glial cells) in response to stress of the endo-lysosomal system, as has been suggested for

neurodegenerative disease contexts (Borland and Vilhardt, 2017; Miranda et al., 2018; Ojha et al., 2017).

(D-F) Autophagic vacuoles (visualized with GFP::LGG-2) in a representative wild-type AIY neuronal soma (D), in an *atg-4.2(ola316)* mutant soma (E), and in an *atg-4.1(bp501)* mutant soma (F). Arrowheads denote autophagic vacuoles in the neuronal soma.

(G-H) Quantification of the average number of LGG-2 puncta in the synaptic regions (G) or cell bodies (H) in wild-type, *atg-4.1(bp501)* mutant, *atg-4.2(ola316)* mutant, and *atg-4.2(gk628327)* mutant animals. Error bars show standard error of the mean (SEM). *p<0.05 and p****p<0.0001 by one-way ANOVA with Tukey's post hoc analysis. Abbreviation: "ns" is not significant between wild-type animals and indicated mutant animals. The number of neurons examined is shown on each bar. Scoring was done by blindly quantifying maximal projections of confocal z-stacks.

(I) Quantification of the percentage of neurons with LGG-1 puncta in the synaptic regions of AIY in wild-type animals, and three independent alleles of *atg-4.2 (ola316, gk430078,* and *gk628327)* mutant animals. While all alleles of *atg-4.2* mutant animals display an increase in the number of neurons with autophagosomes in the neurite (as compared to wild-type animals), we note that the expressivity of this phenotype (the number of LGG-1 puncta per synaptic region) is low as compared to *unc-16* mutant animals. ****p<0.0001 by Fisher's exact test between wild-type and mutant animals. Error bars show a 95% confidence interval. The number of neurons examined is shown on each bar. Scoring was done by blindly quantifying maximal projections of confocal z-stacks.

(J-Q) Panneuronal visualization of autophagic vacuoles in the head of the worm, outlined with white dashed lines, and labeled by *olaIs58* (Paex-3::egfp::lgg-1) (J, L, N, and P). The confocal micrographs shown here in (J, L, N, and P) include the nerve ring region and the anterior portion of the dorsal nerve cord, with schematics summarizing observations in (K, M, O and Q). Results shown for wild-type animals (J and K), *atg-4.2(ola316)* mutant animals (L and M), *unc-16(ju146)* mutant animals (N and O), and *unc-16(ju146); atg-4.2(ola316)* double mutant animals (P and Q). Note that the phenotypes reported here are consistent with those reported using AIY-specific promoters in Figure 3, indicating that these phenotypes are panneuronal. Arrows refer to autophagic vacuoles in the dorsal nerve cord. In K, M, O and Q, green dots represent LGG-1 clusters within the nerve ring, cell bodies, and dorsal nerve cord.

(R) Quantification of the average number of LGG-1 puncta in the synaptic region of AIY for wild-type animals (green bar), *atg-4.1* mutant animals (navy blue and blue bars), *atg-4.2(ola316)* mutant animals (red bar), and indicated *atg-4.1; atg-4.2* double mutant animals (red and blue or peach and blue striped bars). Error bars show standard error of the mean (SEM). The numbers on the bars represent number of neurons examined; corresponding to ≥10 animals for each genotype. Abbreviation: "ns" is not significant as compared to wild-type animals by one-way ANOVA with Tukey's post hoc analysis. Scoring was done by blindly quantifying maximal projections of confocal z-stacks. Corresponding analysis of the cell bodies is shown in Figure 4E.

Scale bar(s): in (A) for (A)-(C); in (D) for (D)-(F); in (J) for (J), (L), (N), and (P).

Figure S5

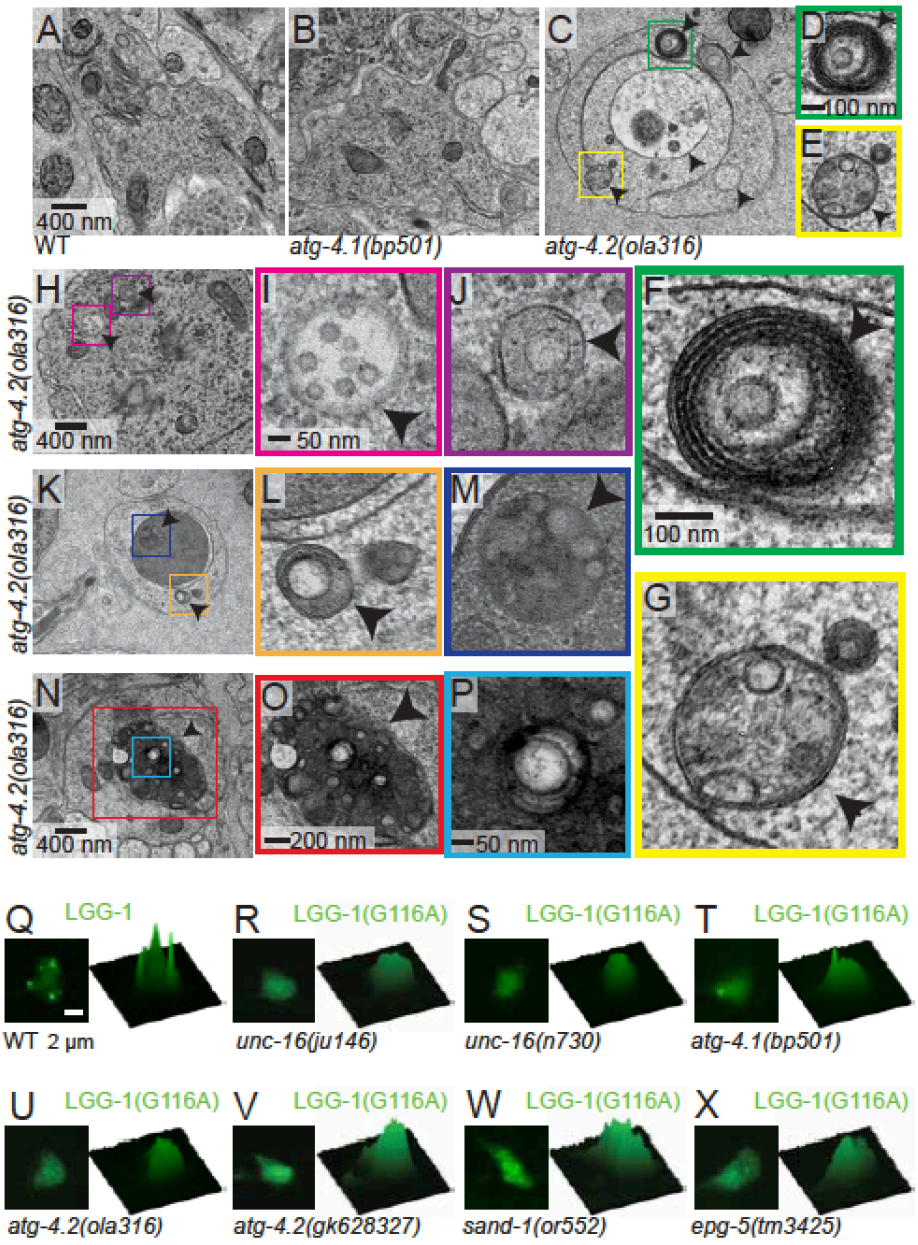

Figure S5. Ultrastructural analyses reveal multilamellar autophagic structures in *atg-4.2* mutant animals, but mutant animals do not contain structures in lipidation control LGG-1(G116A), related to Figure 4.

(A-C) Representative micrographs obtained by electron microscopy of neuronal cell bodies in wild-type animals (A), *atg-4.1(bp501)* mutant animals (B) and *atg-4.2(ola316)* mutant animals (C), as in Fig 4F-4H but without pseudo-coloring.

(D-G) Enlargement of boxed areas showing multilamellar autophagosome-like vacuole examples from (C) are shown in (D and E) and further enlarged in (F and G). These images correspond to the pseudo-colored imaged in Fig 4I and 4J).

(H-P) Additional examples obtained by electron microscopy of neuronal cell bodies in *atg-4.2(ola316)* mutant animals. Enlargements of boxed areas from (H) in (I and J); from (K) in (L and M); from (N) in (O and P). Note the variety in abnormal autophagosome-like vacuolar structures observed. These types of structures were not observed for the other examined genotypes.

(Q-X) Neuronal cell bodies expressing GFP::LGG-1 (Q) or GFP::LGG-1(G116A) (R-X) in representative confocal micrographs (left) and corresponding surface plots (right) for wild-type animals (Q), *unc-16(ju146)* mutant (R), *unc-16(n730)* mutant (S), *atg-4.1(bp501)* mutant (T), *atg-4.2(ola316)* mutant (U), *atg-4.2(gk628327)* mutant (V), *sand-1(or552)* mutant (W), and *epg-5(tm3425)* mutant (X) animals. GFP::LGG-1(G116A) is a lipidation control which does not associate with autophagosomes (also see Figure 1F and S1A-S1F). In the lipidation control GFP::LGG-1(G116A), we observed less than one puncta per cell body in wild type and mutant animals. Animals mutant for *unc-16(ju146)* (0.1 puncta; n=19 neurons), *unc-16(n730)* (0.1 puncta, n=19 neurons), *atg-4.1(bp501)* (0.6 puncta; n=14 neurons), *atg-4.2(ola316)* (0.3 puncta; n=17 neurons), *atg-4.2(gk628327)* (0.1 puncta; n=14 neurons), *sand-1(or552)* (0.1 puncta; n=16 neurons), and for *epg-5(tm3425)* (0.8 puncta; n=16 neurons) all display significantly less puncta than observed for GFP::LGG-1 (3.9 puncta; n=65 neurons; data from Figure 3E). These data suggest that nearly all of the puncta we observe with LGG-1 in wild-type and mutant animals are lipidated.

Scale bar(s): in (A) for (A)-(C); in (D) for (D) and (E); in (F) for (F) and (G); in (H) for (H) and (K), in (I) for (I), (J), (L) and (M); in (N) for (N); in (O) for (O); in (P) for (P); in (Q) for (Q)-(X).

Figure S6

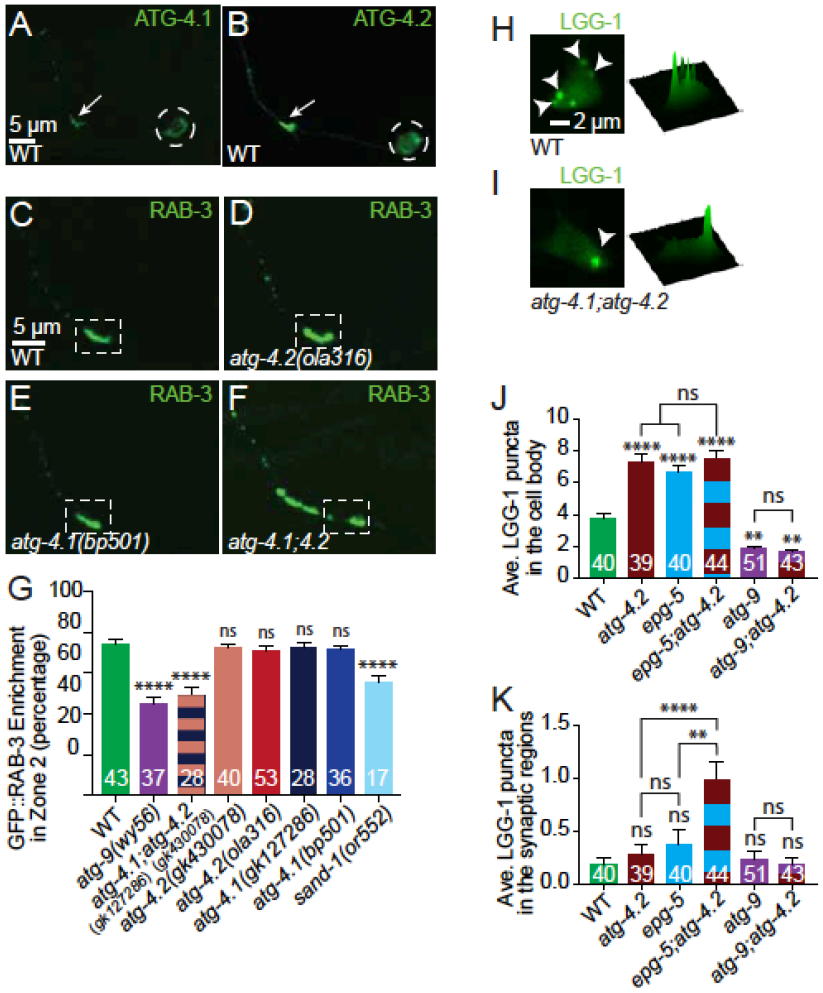

Figure S6. The autophagy proteases *atg-4.1* and *atg-4.2* are partially redundant, and *atg-4.2* acts with *epg-5* to promote autophagic maturation, related to Figure 5.

(A-B) The ATG-4 cysteine proteases, expressed cell specifically in AIY as ATG-4.1::GFP (A) and ATG-4.2::GFP (B), localize similarly along the AIY neurite, including in the synaptic region (arrow) and in the cell body (dashed circle).

(C-F) Representative confocal images of presynaptic structures in AIY (visualized with GFP::RAB-3 to label synaptic vesicles) in wild-type animals (C), *atg-4.2(ola316)* mutant (D), *atg-4.1(bp501)* mutant (E), and *atg-4.1(gk127286); atg-4.2(gk430078)* double mutant (F) animals. The dashed box encloses the synapse-enriched zone 2 region of the neurite, which displays a continuous pattern of synaptic vesicles in wild-type animals. In *atg-4.1; atg-4.2* double mutant animals, but not in *atg-4.1* or *atg-4.2* single mutant animals, note a disrupted pattern of synaptic vesicles representative of synaptogenesis defects (for more descriptions of this phenotype please see (Stavoe et al., 2016)).

(G) Quantification of the percentage of animals displaying a normal synaptic pattern (synaptic enrichment) in Zone 2 of the AIY neurite in wild-type, *atg-9(wy56)* mutant, *atg-*

4.1(gk127286); atg-4.2(gk430078) double mutant, *atg-4.2(gk430078)* mutant, *atg-4.2(ola316)* mutant, *atg-4.1(gk127286)* mutant, *atg-4.1(bp501)* mutant, and *sand-1(or552)* mutant animals. Error bars show standard error of the mean (SEM). ****p<0.0001 by one-way ANOVA with Tukey's post hoc analysis between wild-type and mutant animals. Abbreviations: "ns" is not significant as compared to wild-type neurons. Numbers on bars represent number of neurons examined.

(H and I) GFP::LGG-1 puncta in the AIY cell body imaged as maximal projection of confocal z stacks (left) and corresponding surface plots of the LGG-1 signal intensity (right) in wild-type (H), and *atg-4.2(gk430078); atg-4.1(bp501)* double mutant animals (I). Arrowheads denote autophagosomes in the cell body. Corresponding quantifications are in Figures 4E and S4R.

(J and K) Quantification of the average number of LGG-1 puncta in the cell body (J) and synaptic region (K) of AIY for wild-type (green bar), *atg-4.2(gk628327)* mutant (maroon bar), *epg-5(tm3425)* mutant (blue bar), *epg-5(tm3425); atg-4.2(gk628327)* double mutant (maroon and blue striped bar), *atg-9(wy56)* mutant (purple bar), and *atg-9(wy56); atg-4.2(gk628327)* double mutant animals (purple and maroon striped bar). Error bars show standard error of the mean (SEM). **p<0.01 and ****p<0.0001 by one-way ANOVA with Tukey's post hoc analysis between wild-type and mutant animals or as indicated. The numbers on the bars represent number of neurons examined. Abbreviation: "ns" is not significant between wild-type and mutant animals or as indicated. Scoring was done by blindly quantifying maximal projections of confocal z-stacks. Note that the *atg-4.2; epg-5* double mutant animals do not further enhance AV accumulation in the neuronal soma, but do enhance puncta in the synaptic region. Also note that in animals mutant for the autophagosome biogenesis gene *atg-9*, we observed reduced puncta, which was phenocopied in the *atg-4.2; atg-9* double mutant animals.

Scale bar(s): in (A) for (A) and (B); in (C) for (C)-(F); in (H) for (H) and (I).

Figure S7

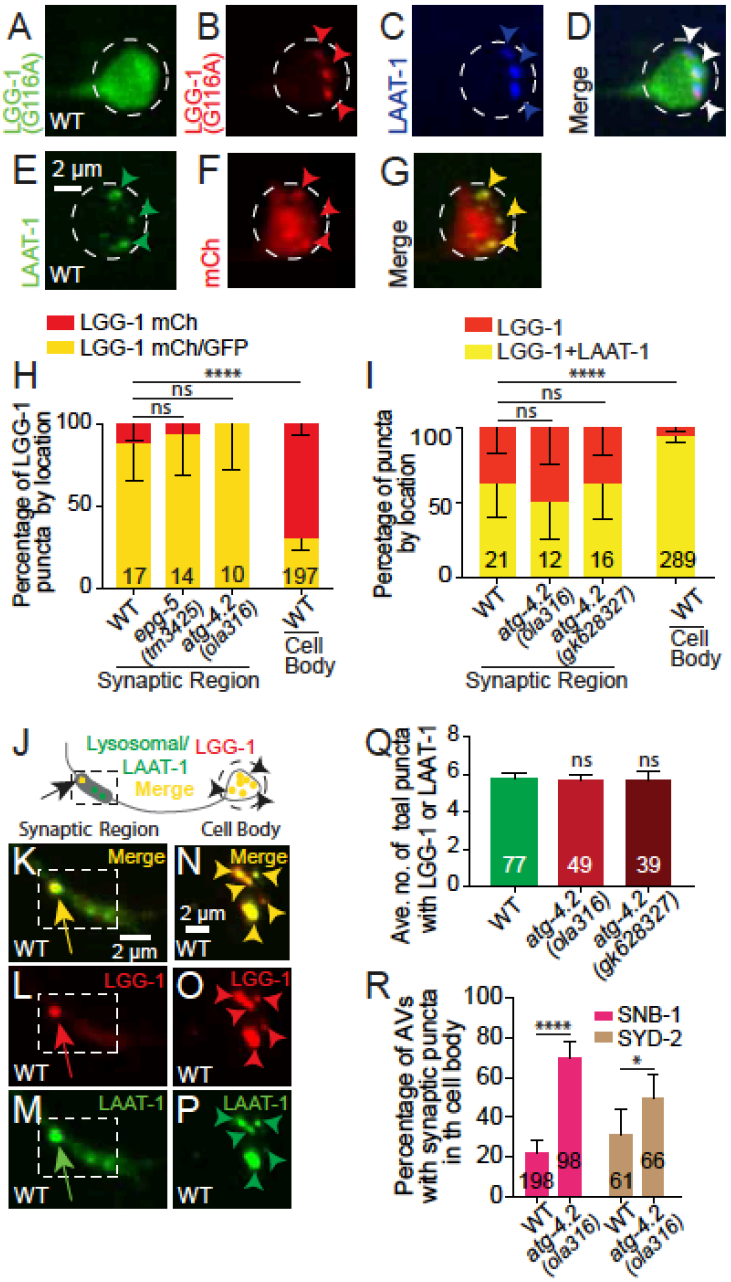

Figure S7. Autophagic structure maturation in the synaptic regions and cell bodies of wild-type and *atg-4.2* mutant animals, related to Figure 6.
(A-D) Lipidation control for tandem LGG-1 marker (mCh::eGFP::LGG-1(G116A)), and lysosomes (LAAT-1::tagBFP) were visualized in the AIY cell body of a wild-type animal. Note that the GFP signal was mostly cytoplasmic (an average of 0.1 puncta per cell body, n=27 neurons) as expected and similar to GFP::LGG-1(G116A) (Figures S1 and S5). We note that we detected mCh puncta in the cell body with the tandem lipidation control marker (4.8 puncta; n=27 neurons, compared to 6.6 mCh positive/GFP negative puncta; n=52 neurons in wild type tandem marker, mCh::eGFP::LGG-1). These were not cytosolic protein aggregates (were they protein aggregates, we would expect to also see

aggregation of GFP). Instead, we observed that most of these mCh puncta colocalized with lysosomal marker LAAT-1::tagBFP puncta (3.6 puncta; n=27 neurons). Indeed, mere expression of cytosolic mCherry results in its accumulation in lysosomes (see E-G). Our data suggest that most non-lipidated mCh puncta are inside acidic lysosomes. Our data are consistent with previous reports of the persistence of mCh in acidified structures (Han et al., 2014; Katayama et al., 2008), see also E-G). Since the non-lipidated mCh structures are acidified and the immature GFP positive structures are lipidated, the tandem marker can be used to assess acidification state. Also see the STAR Methods for additional details.

(E-G) Lysosomes (visualized with LAAT-1::GFP) (A) colocalized with mCherry puncta (B) from cytoplasmically-expressed mCherry (and as seen in the merge image (C)). These findings indicate that mere expression of mCherry results in accumulation of this fluorophore in lysosomes. Arrowheads refer to puncta in the cell bodies. Note that 81% (n=27 puncta from 9 neurons) of cytosolic mCh puncta colocalized with LAAT-1::GFP, similar to the 78% of mCh puncta from the mCh::GFP::LGG-1(G116A) marker shown in (A-D) and suggesting that mCherry persists in acidified structures (Han et al., 2014; Katayama et al., 2008).

(H-I) Quantification of puncta labeled with the LGG-1 tandem marker (mCh::GFP::LGG-1) (H) or with mCh::LGG-1 and/or LAAT-1::GFP (I) in the cell body and synaptic regions of wild-type and mutant neurons, as indicated. Error bars show a 95% confidence interval. ****$p<0.0001$ by Fisher's exact test between indicated groups. Abbreviation: "ns" is not significant between indicated groups. The numbers on the bars represent number of puncta examined from ≥24 neurons for each genotype. Scoring was done by blindly quantifying maximal projections of confocal z-stacks. Note that autophagic vacuoles in the synaptic regions are more immature (GFP/mCh tandem marker signal (H) and lacking LAAT-1 signal (I)), while autophagic vacuoles in the cell body are more likely to be mature (LGG-1 mCh only for the tandem marker (H) and co-labeled with LGG-1 and LAAT-1(I)).

(J-P) Schematic of AIY with the cell body and the proximal portion of the synaptic region, with LAAT-1 (green), LGG-1 (red) and co-labeled structures (yellow) (J). In (K-P), confocal micrographs of LGG-1 puncta (L and O), LAAT-1 puncta (M and P), and co-labeled puncta (K and N), in the synaptic region (K-M) and cell body (N-P) of representative wild-type AIY neurons. Arrows denote puncta in the synaptic region; arrowheads denote puncta in the cell body.

(Q) Quantification of the average of the total number of puncta labeled with mCh::LGG-1, LAAT-1::GFP, or both per AIY cell body in wild-type and *atg-4.2* mutant neurons. Error bars show standard error of the mean (SEM). Abbreviation: "ns" is not significant as compared to wild-type animals by one-way ANOVA with Tukey's post hoc analysis. Scoring was done by blindly quantifying maximal projections of confocal z-stacks. The numbers on the bars represent number of neurons examined.

(R) Quantification of the percentage of autophagosomes (mCh::LGG-1) displaying co-localization with the presynaptic protein GFP::SNB-1 (pink bars) or GFP::SYD-2 (brown bars) in the cell body of AIY interneurons in wild-type or *atg-4.2* mutant animals. Error bars show a 95% confidence interval. ****$p<0.0001$ and *$p<0.05$ by Fisher's exact test between wild-type and mutant animals. The numbers on the bars indicate the number of

puncta scored; corresponding to ≥13 neurons for each genotype. Abbreviations: “AVs” is autophagic vacuoles. Quantification was done by blindly scoring maximal projections of confocal micrographs.

Scale bar(s): in (A) for (A)-(G); in (K) for (K)-(M); in (N) for (N)-(P).

Movie Legend

Movie S1, Time-lapse of autophagosomes in the neurite of an *atg-4.2; unc-16* double mutant animal, related to Figure 3.
Time-lapse video of GFP::LGG-1 in an *atg-4.2(ola316); unc-16(ju146)* double mutant AIY neuron showing accumulated structures trafficking inside and outside of the AIY neuronal process.

Table S1, related to STAR Methods

Oligonucleotides		
Genotyping primer: *atg-4.2(ola316)*-F ACACTGCCATGCTTCTATCAATCG	This paper	N/A
Genotyping primer: *atg-4.2(ola316)*-R CATCAGACAGACACCTTTCATCCC	This paper	N/A
Genotyping primer: *atg-4.2(gk628327)*-F TCAGAGTATTCGGCCATAGAAAG	This paper	N/A
Genotyping primer: *atg-4.2(gk628327)*-R GCAGCAATTCCAACCATCTTATG	This paper	N/A
Genotyping primer: *atg-4.2(gk430078)*-F CCTCATTATCAGATGATGATGGACACG	This paper	N/A
Genotyping primer: *atg-4.2(gk430078)*-R GCAATCTATGCCTACCTAGTCGC	This paper	N/A
Genotyping primer: *atg-4.1(bp501)*-F ACGTGGACGGCGATATTCGAC	This paper	N/A
Genotyping primer: *atg-4.1(bp501)*-R GGTTTAGCCTCTACCAAATGAATCGG	This paper	N/A
Genotyping primer: *atg-4.1(gk127286)*-F GACTGAAGCCTACGTCATCGG	This paper	N/A
Genotyping primer: *atg-4.1(gk127286)*-R CAGAAAACGGCCTCGTCGAC	This paper	N/A
Genotyping primer: *sand-1(or552)*-F TCTGTCTGCCACGGTTCAATG	This paper	N/A
Genotyping primer: *sand-1(or552)*-R CGACGCATTTCTGAACGAGCA	This paper	N/A
Genotyping primer: *epg-5(tm3425)*-F WT CTTACTGGAATGGCAGTAGCTGAGTGTG	This paper	N/A
Genotyping primer: *epg-5(tm3425)*-F mut GTGGCAAAGGAGGAATATACCGTCGTC	This paper	N/A
Genotyping primer: *epg-5(tm3425)*-R CAGCGTGTTTCTCAAGAAAGAGAAGCTCC	This paper	N/A